eman ta zabal zazu

Universidad del País Vasco
Euskal Herriko Unibertsitatea

Optoelectronic properties in heterostructures of 2-dimensional materials

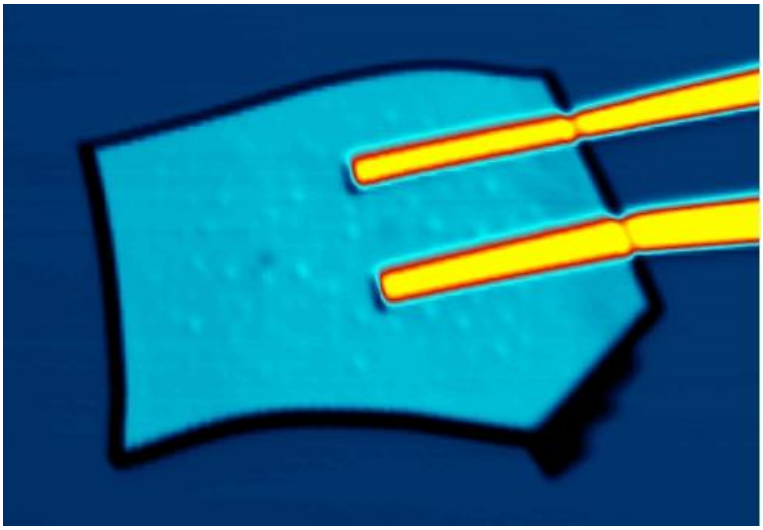

DOCTORAL THESIS IN
Physics of Nanostructures and Nanomaterials
submitted by

María Nieves Morquillas Azpiazu

Supervised by José Ignacio Pascual Chico

San Sebastian, JUNE 2018

(c)2018 MARIA NIEVES MORQUILLAS AZPIAZU

This thesis has been carried out at CIC nanoGUNE

"Don't you cry for the lost, smile for the living!
Get what you need and give what you're given!
Life's for the living so live it or you're better off dead"

Michael David Rosenberg

Acknowledgments

The four years of PhD has never been a lonely and isolated journey. Without the support, patience and guidance of the following people, this work would not have been accomplished. It is to all of you that I owe my deepest and most sincere gratitude.

First, I would like to thank and express my deepest gratitude to my supervisor **Nacho** and **Doktorvater, Herr Pascual**.

Scientifically, I can just feel very grateful for your guidance, kind support and considerable encouragement taking out the best of me. Also, for the opportunity of being in nanoGUNE. It has been very appealing to work surrounded by such hard-workers.

Thank you for being also a Doctor Father and support me during the several hard moments I faced in the last years. Your door was always open during these 5 years for both science and life learning.

"Tener muy claro dónde queremos llegar e ir directos hacia ello"

I am also greatly thankful to the reading committee of my thesis. Thank you for carefully reading my thesis and providing me with valuable scientific comments.

I am greatly thankful to all the colleagues of the **CIC09** group. Una de las primeras personas que conocí al llegar a nanoGUNE fue **David**. Gracias por ser el mejor técnico que se puede tener, por las risas y las broncas y porque sabes que me voy en un mes y me vas a echar muchísimo de menos! Al que mejor se conoce la entrada de nanoGUNE, **Javi**. Gracias por estar siempre ahí, escuchando y apoyando en cada situación. Abrígate! I would also like to thank the ungraduated students that have worked with me during these years (**Robert** and **Mikel**). Their work contributed to this thesis and the development of other skills. **Martina** and **Zsolt** because you were the first friendly faces I saw when I arrived to CIC09. **Carmen, Nerea, Edu y Nestor** por todos los buenos momentos durante estos años.

And of course to everyone else in the group, members and visitors along these years: **Richard, Miguel, DJ, Li, Nestor, Jeremy, Claudia, Oscar, Mikeles, Ana, Oscar, Joeri, Rene, Alex, Lei, Maciej, Niklas, Reyes and Anil**.

I extend this to ALL **nanoPEOPLE**. Thank you for creating the best working and relaxing atmosphere because your character and help is long away from NANO. A good thing of being for 5 years in the same place is getting to know so many different people.

From the optics group to **Stefan** for the help in the lab whenever I need it and always with a huge smile in the face. Also, for your friendship and the beer-philosophy discussions to fix the world. Also to **Rainer** for the opportunity to learn a bit from the near field optics world in a really high scientific atmosphere and the scientific discussions that stimulated great ideas.

From the nanodevices group to **Saül**. Gracias por guiarme en mis primeros pasos de exfoliación. También por las horas de EBL dedicadas a poner contactos a mis muestras hasta tu último día en nanoGUNE. A **Juanma** por heredar el poner contactos a mis muestras siempre con una sonrisa en la cara y feliz de trabajar.

Stephanie Reig, thank you for a fantastic time in Berlin where I learned a lot about optics and specially about polarized light. **Patryk, Soeren and Georgi** and the rest of the group at the Freie Universität Berlin for such a great experience for both science and city life.

From my San Sebastian family, I would like to thank the DIPC and CFM **PhD folks**, thanks for the scientific discussions as well as for all the good moments (pizza/pintxo-potes, beers, chuletas, laughs...) and support for the last 5 years (**Berni, Dino, Fra, Ivor, Moritz, Jorge, Lars, Bruce, Miguel, Tomas, Andrea, Josu, Alvaro**).

Last but not least... Creo que no tengo suficientes palabras de agradecimiento para algunas personas.

Gracias **chics** por vuestro apoyo constante. Estar en los buenos momentos es fácil pero es en los difíciles cuando siempre aparecéis. En definitiva, gracias por ser ls mejors amigs que alguien puede tener.

Al **best English student**, por ESTAR y ayudarme a hacer una versión más madura de mi misma, por la fuerza que me trasmites. En definitiva por hacerme feliz, creo que no se le puede pedir más a una persona **ESKERRIK ASKO TEAM-mate! ;)**

A Mamá, Papá, Pilar, Jose y Luis por TODO lo que soy.

Por último, a ti Abu porque hacías mucha falta y no pasa un día sin echarte de menos, me habría encantado enseñarte esta tesis. Intentaré tener siempre presente cómo le gustan a la abuela las niñas.

Simplemente ¡GRACIAS familia, que de eso solo hay una!

With my eyes full of tears of gratitude:

¡MUCHÍSIMAS GRACIAS A TODOS! THANK YOU ALL!!

Abstract

Transition metal dichalcogenides (TMD) MX_2 (M=Mo, W, Nb; X= S, Se, Te) are promising materials for optoelectronic applications due to their exceptionally tunable properties. Monolayers (1L) of some TMDs present different optical and electrical properties than bulk. In the single-layer limit, MoS_2 and WSe_2 behave as a direct-gap-like semiconductor, whereas bulk MoS_2 and WSe_2 are indirect-gap-like semiconductor. This difference, which comes from a change of the electronic band structure with thickness, gives to higher photoluminescence quantum efficiency in the single-layer regime.

Another interesting property of these materials appears as a consequence of the inversion symmetry breaking for an odd number of layers. The broken symmetry and the strong spin orbit coupling (SOC) in the single layer limit make the gaps in K and K′ point distinguishable. Therefore, the electrons are described not only by their charge and spin but also by the extra degree of freedom called "valley". This gave raise to a new field with applications in information encoding and processing, called "valleytronics". Most of the research lines efforts are devoted to obtain valleytronic devices able to produce a current coming exclusively from one of the valleys.

The properties of single layer TMDCs can be also highly affected by the interaction with the substrate where they are deposited. Here, we study the optical and electrical properties of 1L-MoS_2 and 1L-WSe_2 on top of a superconductor and an insulating ferrimagnetic material respectively. In the first case, we aim to study the properties of a superconductor semiconductor junction. Our structures are formed by 1L-MoS_2 deposited on top of a bulk like $NbSe_2$, all in a SiO_2 substrate. $NbSe_2$ is a superconductor with Tc=7 K. Above this temperature, $NbSe_2$ behaves as a normal metal and the hybrid presents a typical Schottcky barrier.

However, below the critical temperature the resistance of $NbSe_2$ drops to zero and we can study the formation of a super Schottky barrier. In the second case, we explore the properties of 1L and few layer flakes (MoS_2 and WSe_2) on top of a ferrimagnetic substrate (Yttrium Iron Garnet-YIG). In these samples, we study the effect of the inhomogeneous magnetic texture of the substrate on the valley exciton transitions of the MoS_2.

We study the optoelectronic properties by combined luminescence and electronic transport measurements, at room and low temperatures. Since the substrate could modify not only the electron but also the phonon properties of MoS_2, heterostructures are also studied by Raman Spectroscopy under different excitation wavelengths and temperatures. To determine the role of the substrate, results are compared to those of samples deposited on SiO_2 substrate.

Resumen

Esta tesis presenta un estudio detallado de las propiedades optoelectrónicas de materiales confinados en 2 dimensiones. Principalmente se estudian materiales de la familia de los dicalcogenuros de metales de transicion (TMDs). Las propiedades de estos materiales se pueden modificar con relativa facilidad por lo que actualmente aparecen como el futuro en campos de gran impacto social como puedan ser la conversión de energía, el almacenamiento y codificación de la información o en telecomunicación [1–11].

Muchos de los materiales 2D como por ejemplo el grafito o la molibdenita (MoS_2) son minerales que existen en la naturaleza. El hecho de confinarlos en dos dimensiones modifica sus propiedades ópticas, eléctricas y mecánicas, aumentando el número de posibles aplicaciones. Un gran número de estos materiales 2D pertenecen a la familia de los dicalcogenuros de metales de transición (TMDs) [12–14, 14, 15]. Los TMDs responden a una estequiometría MX_2 en la que M corresponde a un metal de transición (Mo, W, Nb, V) y X a un elemento del grupo de los calcógenos (Se, S o Te). Los diferentes materiales tiene una estructura cristalina triangular en la que el elemento metálico se encuentra embebido entre dos capas del elemento calcógeno. Los diferentes elementos se unen entre sí por enlaces covalentes fuertes, mientras que la unión entre las diferentes capas se produce mediante fuerzas de Van der Waals más débiles. Esto permite aislar mono-capas de estos materiales mediante exfoliación mecánica.

Para estudiar las propiedades optoelectrónicas de los TMDs, hemos realizado varios dispositivos con MoS_2 como semiconductor. Inicialmete, hemos fabricado dispositivos conectando una mono-capa de MoS_2 con dos contactos metálicos para caracterizar la formación de las barreras de potencial. Una de las formas de aumentar la eficiencia de los dispositivos es restringiendo la dirección de la corriente en un sentido, aumentando el ratio entre la parte que conduce y la rectificadora. Esto se puede conseguir creando barreras de potencial en los dispositivos mediante la combinación de diferentes materiales. En esta tesis creamos dos tipos de heteroestructuras. La primera creada contactando una lámina multi-capa de MoS_2 y la otra formada por una mono-capa de MoS_2 depositada encima de una lámina con

varias capas de $NbSe_2$. Se establece una conexión entre las láminas mediante contactos de Cr/Au. Los procesos de escritura de los contactos se realizan mediante un proceso de litografía con electrones (EBL por sus siglas en inglés) y la posterior deposición de Cr y Au como metales de contacto. Esta parte de la fabricación de las muestras la llevaron a cabo Saül Velèz y Juan Manuel Gómez del grupo de Nanodevices de nanoGUNE.

El cambio de las propiedades ópticas de estos materiales se puede utilizar para detectar el número de capas. La espectroscopía Raman es una técnica muy extendida para realizar esta caracterización sin dañar el material. En MoS_2 lo separación de los picos correspondientes a los modos E^1_{2g} y A_{1g}, aumenta con el número de capas (Figura 1-a) [16–18]. En el caso del WSe_2 el ratio entre los principales modos (E^1_{2g}/A_{1g}) aumenta con el número de capas hasta que llega a un valor máximo (Figura 1-b) [16, 17]. El $NbSe_2$ es un material que se oxida con relativa facilidad. El óxido de este material hace que los modos de vibración activos en Raman disminuyan (E^1_{2g} y A_{1g}) y aparezca un nuevo modo de vibración (Figura 1-c) [19].

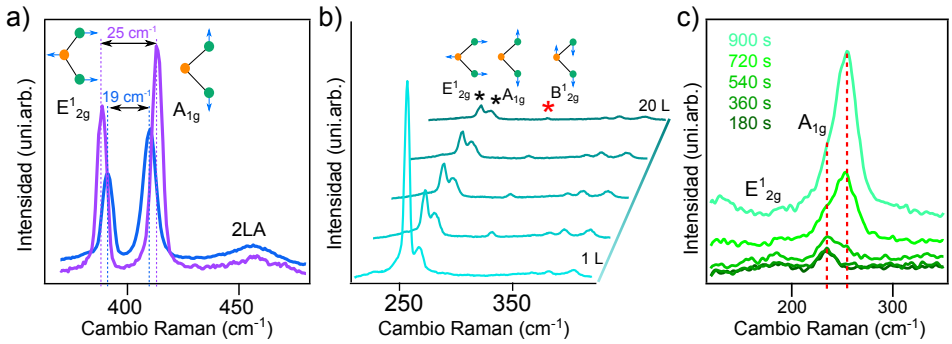

Figure 1: a) Espectro de Raman tomado en una lamina con 1 y 6 capas de MoS_2. b) Espectro de Raman de WSe_2 con diferente número de capas 1 a 20. c) Evolución temporal del espectro de Raman del $NbSe_2$. Todos los espectros en esta figura se miden con una excitación de 532 nm.

Las propiedades ópticas del MoS_2 cambian con el confinamiento. La molibdenita es un semiconductor con un gap indirecto pero al disminuir el número de capas se produce un cambio en la estructura de bandas del material y el gap pasa a ser directo (Figura 2-a) [20–22]. Este cambio aumenta la eficiencia cuántica de la fotoluminiscencia en varios ordenes de magnitud (Figura 2-b). Es interesante ver como a baja temperatura el espectro de fotoluminiscencia cambia de intensidad y apariencia dependiendo del material. Estos cambios están directamente relacionados con la estructura de bandas de cada material. Por ejemplo, para el WSe_2 es posible resolver diferentes picos de emisión producidos por excitones o triones [23].

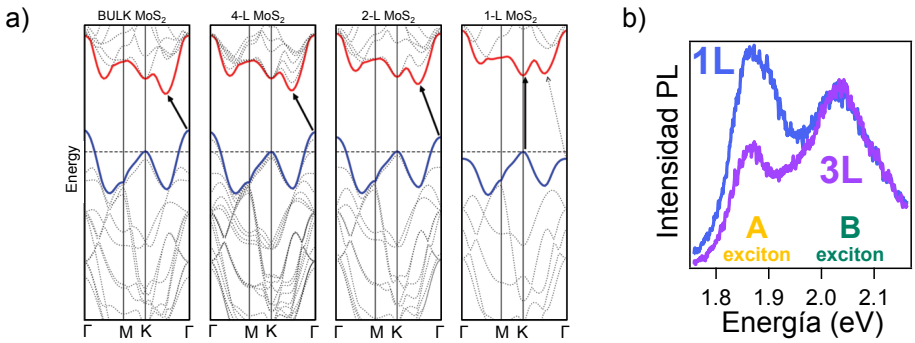

Figure 2: a) Diagrama de bandas del MoS_2 calculado para el cristal, 4, 2 y 1 capa. Las flechas indican la transición de menor energía. Esta figura es una adaptación de [22]. b) Espectro de fotoluminiscencia correspondiente a 3 y 1 capa de MoS_2.

La caracterización óptica y eléctrica de los diferentes materiales se realiza principalmente mediante microscopía confocal. Para ello, se equipa el microscopio con un multímetro digital capaz de analizar la señal eléctrica y un espectrofotómetro con con una camara CCD (por sus siglas en inglés, Charge Coupled Device) acoplada, que analiza la señal óptica. En el camino óptico es posible añadir diferentes componentes para realizar medidas de polarización de la luz con el fin de estudiar el grado de libertad del valle. La microscopía confocal es una técnica óptica en la cual la resolución espacial viene determinada por el límite de difracción. Por ello, también se ha medido la fotocorriente de algunos dispositivos con un microsopio de campo cercano (SNOM). La microscopía de campo cercano mide la señal reflejada por una punta de AFM. Por ello, la resolución espacial en esta técnica viene dada por el tamaño de la punta y no por la longitud de onda. En una colaboración con el grupo de Nanoóptica en nanoGUNE, se equipó este microscopio con un espectrofotómetro y un detector CCD [24]. De esta forma conseguimos detectar las señales ópticas y eléctricas de forma casi simultánea mediante una técnica conocida como *tip enhanced spectroscopy*.

Al poner en contacto un semiconductor con un metal se produce una transferencia de electrones de un material a otro. La migración de la carga está directamente relacionada con la función de trabajo del metal y con la afinidad electrónica y tipo de dopaje del semiconductor. En el caso de dispositivos de MoS_2 (semiconductor de tipo n) conectado con contactos metálicos de Cr/Au, se produce una migración de electrones hacia el metal, produciendo una disminución del número de electrones en el semiconductor. Esto genera un potencial que decrece en la dirección del semiconductor, creando un área de disminución de carga (W) [25, 26]. La presencia de

defectos capaces de atrapar electrones en ellos o la existencia de estados localizados produce una desviación de la descripción ideal de la formación de la barrera. Esta desviación viene dada principalmente por una fijación del nivel de Fermi del semiconductor a una energía determinada promovida por los defectos [27–29].

En semiconductores es posible excitar electrones desde la banda de valencia a la banda de conducción mediante su iluminación, generando un par electrón-hueco. Estos pares tiene dos mecanismos de recombinación, de forma radiativa o no radiativa. Sin embargo, bajo una determinada diferencia de potencial existe una cierta probabilidad de que estos pares electrón-hueco se separen y difundan siguiendo la caída de potencial. Los electrones extras así generados producen un aumento de la corriente del dispositivo.

En los dispositivos de una mono-capa de MoS_2, observamos corriente de electrones para ambas polaridades debido a la simetría del dispositivo. Lo singular, es que la fotocorriente se genera mediante procesos diferentes dependiendo de la posición del laser (Figura 3-a). En la zona central del dispositivo no hay una caída de potencial, por lo que es necesario aplicar un V_{sd} para generar fotocorriente, fotoconductividad. Por el contrario, en zonas cercanas a los contactos la caída de potencial permite que el par electrón-hueco se separe, produciédose un aumento de la intensidad de corriente, efecto fotovoltaico (Figura 3-b) [30]. El cambio en la energía del gap y del grado de dopaje del MoS_2 con el número de capas, hace que se genere una barrera de potencial (unión nN) en la unión entre las diferentes capas. Esta barrera de potencial hace que la corriente solo pueda fluir en una dirección creando una respuesta rectificadora (Figura 3-c) [8].

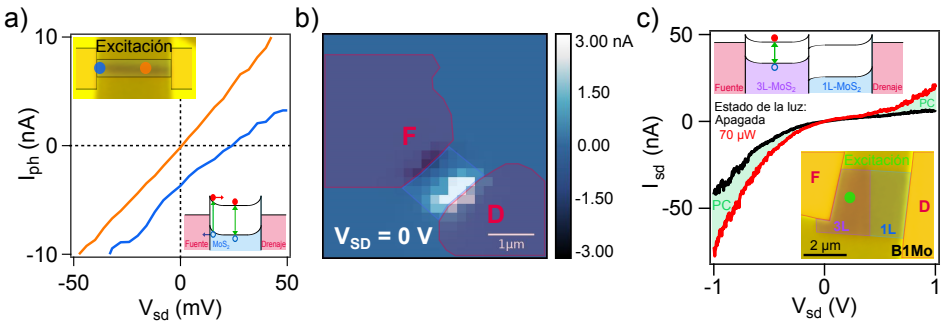

Figure 3: a) Evolución de la fotocorriente a bajos V_{sd} con la iluminación cerca del contacto metálico (azul) y en el centro del dispositivo (naranja). b) Mapa de fotocorriente a $V_{sd} = 0$ V c) Curva de corriente-voltaje de un dispositivo con 3 y 1 capa de MoS_2 sin iluminación y con excitación con un laser verde.

Por último, se han estudiado heteroestructuras creadas a base de MoS_2 y $NbSe_2$ (Figura 4-a). El $NbSe_2$ es un aceptor fuerte de electrones, por lo que se esperaba que se produjera una barrera de potencial alta en contacto con el semiconductor. En la heteroestructura el MoS_2 es atómicamente fino por lo que en la dirección perpendicular al plano no hay material para que se recupere la estructura de bandas. Por ello, en la zona de la heteroestructura el MoS_2 aparece con un dopaje de tipo p mientras que el resto del material permanece tipo n (diagrama de bandas en la figura 4-a). Dado que todos los materiales en la heteroestructura están en contacto, es posible medir barreras de tipo p-n y tipo n-p-n. Las medidas de corriente y fotocorriente que hemos realizado confirman el diagrama de bandas propuesto y muestran un ratio I_{luz}/I_{oscuro} muy alto de la unión p-n iluminando la heteroestructura (Figura 4-b). Además, se ha calculado la estructura de bandas y la transferencia de carga mediante cálculos de DFT. Los cálculos realizados por Ernesto Ruiz y el Dr. Emilio Artacho confirman la estructura de bandas de la heteroestructura. Sus resultados muestran un dipolo generado en el MoS_2 debido a la transferencia de cargas que produce un movimiento de las bandas del MoS_2, apareciendo con la energía de Fermi en la parte inferior del gap (p-MoS_2) (Figura 4-c). Por último, el $NbSe_2$ es también un superconductor por debajo de 7 K. Por ello, en esta heteroestructura se puede estudiar la barrera de potencial creada entre un semiconductor y un superconductor [31–37]. Desafortunadamente, estos dispositivos presentan una resistencia demasiado alta para detectar corriente a baja temperatura.

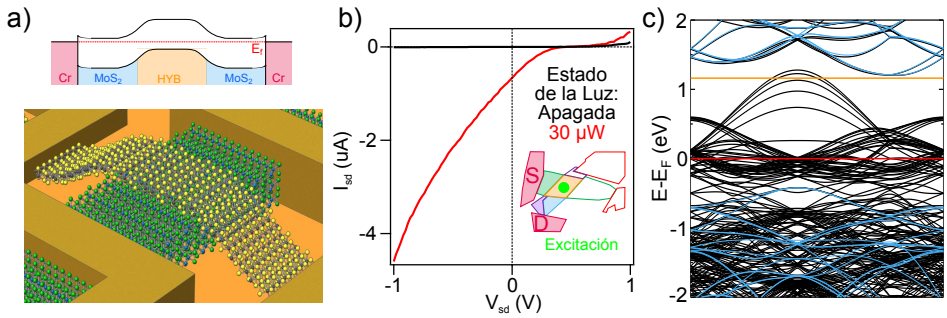

Figure 4: a) Esquema mostrando la heteroestructura hecha de una capa de MoS_2 sobre una lámina gruesa de $NbSe_2$ contactada con contactos de Cr/Au. Imagen hecha por David Arias. b) Curva de corriente-voltaje sin iluminar el dispositivo e iluminando en la heteroestructura (unión p-n). c) Diagrama de bandas de la heteroestructura (negro) con el diagrama de bandas del MoS_2 con un 4% superpuesto (azul). Calculos de DFT realizados por Ernesto Ruiz.

La última parte de esta tesis trata de estudiar el nuevo grado de libertad que aparece en los TMDs semiconductores, el valle. El WSe_2 tiene

una interacción spin-órbita fuerte y la simetría de inversión está rota en la mono-capa. Por ello, en este material las transiciones de los puntos K y K′ de la zona de Brillouin tienen asociadas un momento opuesto protegido por la simetría de inversión temporal [9, 10, 38]. En ausencia de un campo magnético, la única diferencia entre las transiciones producidas en K o K′ es la helicidad de la luz emitida. En presencia de un campo magnético, este se acopla con el momento del orbital d del metal de transición, produciendo una separación de las bandas (Figura 5-a). La separación entre las bandas corresponde a la energía de Zeeman y hace que para una dirección determinada del campo magnético en la dirección perpendicular al plano las transiciones en K y K′ tengan diferente energía (Figura 5-b).

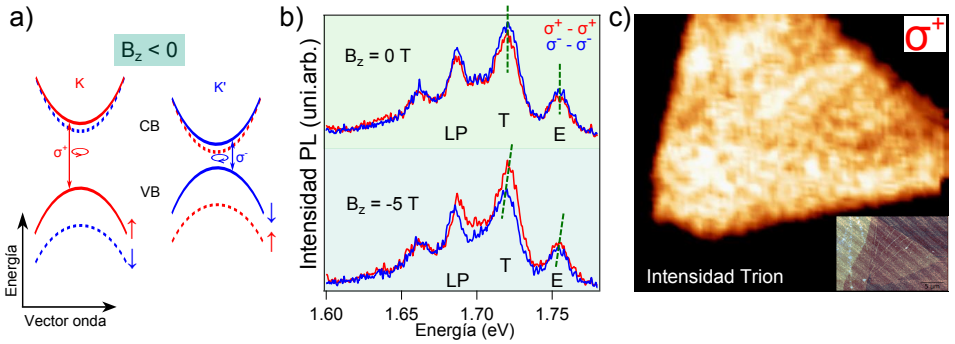

Figure 5: a) Evolución de las bandas en K y K′ bajo el efecto de un campo magnético negativo. b) Espectros de fotoluminiscencia excitando con luz polarizada circularmente bajo un campo magnético. c) Mapa de fotoluminiscencia del trion a 77 K bajo una excitación verde polarizada circularmente. La imagen pequeña muestra una superposición de imagenes de AFM y MFM que muestran la topografía de la lamina de WSe_2 y los dominios magnéticos del sustrato ferrimagnético.

Las medidas las hemos realizado en una mono-capa de WSe_2 sobre un substrato ferrimagnético (YIG, Yttrium Iron Garnet). La idea era correlacionar la estructura de dominios magnéticos del sustrato con un efecto de Zeeman sobre el semiconductor. Hemos conseguido con éxito ver la diferencia de energía al aplicar un campo magnético externo bajo diferentes polarizaciones. Pero no se ha podido correlacionar la señal con la estructura de dominios del substrato ferrimagnético. El substrato utilizado tiene una rugosidad relativamente alta, capaz de producir estrés en el material. Se ha publicado en varios trabajos que un estrés grande sobre este tipo de materiales puede producir un efecto similar a aplicar un campo magnético del orden de 100 T [39–44]. Por ello, la distribución espacial de la energía del excitón sin campo magnético, es relativamente aleatoria (Figura 5-c).

Acronyms and notation

AFM	Atomic Force Microscope
BS	Beam Splitter
CB	Conduction Band
CCD	Charge-Coupled Device
DFT	Density Functional Theory
DOS	Density Of States
EBL	Electron Beam Lithography
EQE	External Quantum Efficiency
FC/APC	Fiber Channel/Angled Physical Contact
FE	Field Emission
GGG	Gadolinium Gallium Garnet
IQE	Internal Quantum Efficiency
IR	Infrared
IPA	Ispropanol
KPFM	Kelvin Probe Force Microscopy
LP	Linear Polarizer
MM	Multi-mode
MIBK	Methyl Isobutyl Ketone
MFM	Magnetic Force Microscopy
NA	Numerical Aperture
PC	Photocurrent
PDMS	Polydimethylsiloxane
PL	Photoluminescence

PMMA	Polymethyl methacylate
PV	Photovoltaic
QE	Quantum Efficiency
QY	Quantum Yield
REG	Rare Earth Garnets
RR	Rectifying Ratio
RT	Room Temperature
SERS	Surface Enhanced Raman Spectroscopy
SM	Single Mode
SNOM	Scanning Near field Optical Microscopy
s-SNOM	scattering-Scanning Near field Optical Microscopy
SOC	Spin-Orbit Coupling
SOS	Spin-Orbit Splitting
SPCM	Scanning Photocurrent Confocal Microscopy
SPM	Scanning Probe Microscopy
TEM	Transmission Electron Microscopy
TFE	Thermionic Field Emission
TEPC	Tip-Enhanced Photocurrent
TEPL	Tip-Enhanced Photoluminescence
TERS	Tip-Enhanced Raman Spectroscopy
TMD	Transition Metal Dichalcogenide
VB	Valence Band
YAG	Yttrium Aluminum Garnet
YIG	Yttrium Iron Garnet

Contents

Chapter 1

Introduction

Since the isolation of a single graphene layer in 2004, materials science has seen the emergence of a new field of research with two-dimensional materials (2D). Bulk materials such as graphite, molybdenite (MoS_2) or paramontroseite (VO_2) are minerals that have been present for many years, but the importance of this family of materials relies on the role of confinement.

Confinement changes the dimensionality of materials, what drastically changes not only their electronic properties but also their vibrational properties (phonons). An example of this is MoS_2. Bulk MoS_2 is an indirect gap semiconductor, whereas an isolated layer of this material behaves as a direct gap semiconductor. Therefore, many of these materials are studied now for different applications than the bulk ones.

The 2D family includes materials with a wide variety of highly-tunable properties, in the nanometer scale. Devices made from this materials have reached higher efficiencies than traditional bulk, macroscopic scale, materials. Therefore, 2D materials are a breakthrough in a wide variety of fields with high social impact, such as energy conversion, information encoding and storage, high-speed communications or detectors, among others.

1.1 Two-dimensional materials

Two dimensional materials have many advantages compared with their peer bulk materials. They have remarkable mechanical, electric and optical properties that can be easily tuned by changing doping, strain, external electric/magnetic field. The high stability of atomically flat layers combined with their high flexibility opens the possibility of integrating single layers in high quality devices, improving the final performance of the device.

2D materials attracted a lot of interest for scientific and technological applications. These materials are used for different applications such as energy and information conversion and storage. More specifically, for plasmonics (h-BN, graphene) [1–3], optoelectronics (graphene, MoS_2, WSe_2) [4–8] and valleytronics (MoS_2, WSe_2) [9–11].

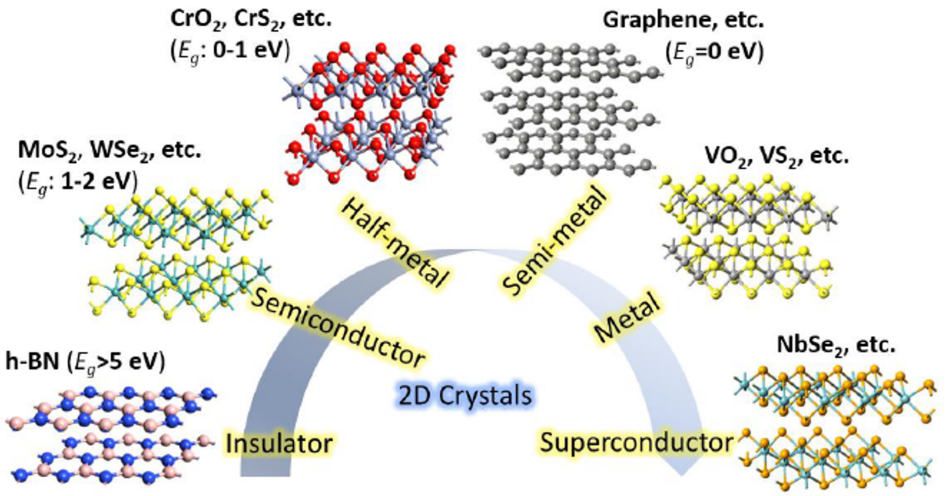

Figure 1.1: Schematic illustration of 2 dimensional materials organized in insulators, semiconductors, half-metals, semi-metals, metals and superconductor. Image adapted from [45].

Their crystalline structure is characterized by strong intra-layer covalent bonds and weak inter-layer Van der Waals interactions. Due to the weak inter-layer interaction, 2D materials can be mechanically exfoliated in order to get single layers (Chapter 2.1). A single layer of a 2D material can be made of 1 atomic layer (graphene), 2 atomic layers (h-BN), 3 atomic layers (MoS_2, WSe_2) or more. Moreover, depending on the elements bonded in the single layer, we can classify the materials as insulators (h-BN), semiconductors (MoS_2, WSe_2), half-metals (CrO_2, CrS_2), semi-metals (graphene), metals (VO_2, VS_2) or superconductors ($NbSe_2$). The biggest family of 2D materials is the transition metal dichalcogenides. In TMDs we find a layer

of transition metal atoms (M = Mo, W, Nb, V,...) embedded in two layers of chalcogenide atoms (X = S, Se, Te), giving an MX_2 stoichiometry. Depending on M and X, can be obtained materials with different electrical and optical properties.

TMDs are very promising materials for optoelectronic devices, mainly due to their larger conductance and optical response compared to their non-2D counterparts. Also, it is important to highlight the high degree of tunability of these materials, allowing band-structure engineering by changing the number of layers or inducing strain on the material [12–14, 14, 15].

Along this thesis we study different TMDs: two semiconductor (WSe_2 and MoS_2) and a superconductor ($NbSe_2$). To study the optoelectronic properties we prepare MoS_2, MoS_2 isotype heterostructure and MoS_2-$NbSe_2$ heterostructure devices. The valley properties are studied for 1L-WSe_2, choosing this material for different experimental reasons that will be described later in this thesis.

1.1.1 Transition metal dichalcogenides

Semiconducting TMDs (MoS_2 and WSe_2): Semiconducting TMDs (MX_2, WX_2) are indirect-gap bulk semiconductors. However, by decreasing the number of layers the gap turns to direct-type with larger energy at the K point of the Brillouin zone. In the single-layer regime inversion symmetry is broken and the large spin-orbit interaction of the atoms induces the spin-splitting of bands located at the inequivalent K and K′ points. The helicity of the two distinguishable valleys at K and K′ related by time reversal symmetry gives the possibility to access and manipulate with electro-magnetic fields the valley (pseudo-spin) degree of freedom.

The energy gap of these material appears in the visible range of the electromagnetic spectrum. As a consequence, the electrons in the valence band (VB) of the semiconductor can be promoted to the conduction band (CB) by optical excitation. Additionally, semiconductor TMDs can be grouped as bright (MX_2) or darkish (WX_2) semiconductors depending on whether the transition allowed by selection rules appears at hight or low temperatures.

Excitons have a relatively long lifetime (hundreds of ps) and large exciton binding energies (few hundreds of meV) compared with other semiconductors, enabling the formation of charge excitons; trions. There are positive trions (1 electron bounded to 2 holes) and negative trions (2 electrons bounded to 1 hole). As excitons, the emission from the trions also follows the selection rules and thus needs to conserve the spin momentum.

In chapter 3, different properties of WSe_2 and MoS_2 are more extensively described and studied by optical spectroscopy.

Superconducting TMDs ($NbSe_2$): $NbSe_2$ is a type-II superconduc-

tor from the family of TMDs materials with a critical temperature (T_c) of 7.2 K [46–48]. Most of the measurements that will be shown in this thesis were performed at room temperature, at which $NbSe_2$ behaves like a strong electron-acceptor metal. The reported work function (ϕ_B) is around 5.9 eV [49], larger than that of other metals (ϕ_{Au} = 5.1 eV, ϕ_{Ti} = 4.33 eV, ϕ_{Cr} = 4.5 eV, ϕ_{Pb} = 4.14 eV) [50, 51].

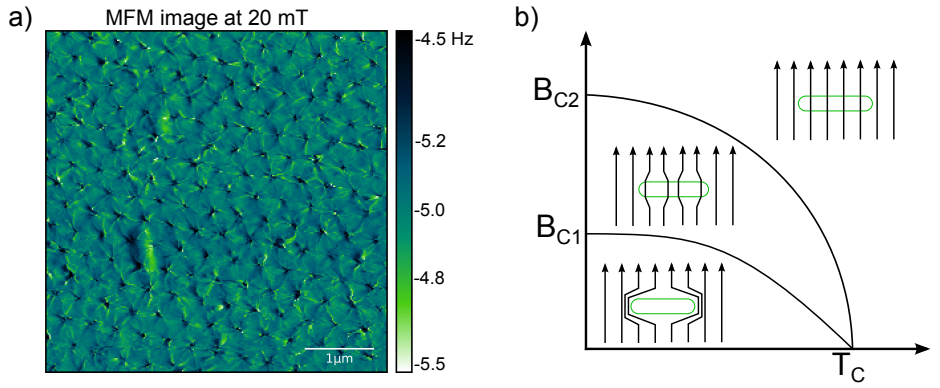

Figure 1.2: a) Magnetic force microscopy image showing the magnetic vortices arranged in the Abricosov lattice. b) Phase diagram of a type II superconductor, repulsion of the magnetic field below H_{c1}, magnetic vortices form between H_{c1} and H_{c2} and no superconductivity above T_c or H_{c2}.

Type II semiconductors are characterized by the formation of magnetic vortices under an external magnetic field (between H_{c1} and H_{c2}) (Figure 1.2-b). Magnetic vortices arrange in a triangular lattice (Abrikosov lattice) and the distance between them depends on the applied magnetic field [47]. The magnetic vortex structure can be measured by magnetic force microscopy (MFM) [52–55] (Figure 1.2-a). Bellow this critical magnetic field, H_{c1}, the superconductor repels the magnetic field. Above T_c or H_{c2}, superconductivity in the material is destroyed. The critical values for T_c, H_{c1} and H_{c2} in $NbSe_2$ also vary as a function of the different number of layers.

Chapter 2

Experimental introduction

During the last few years there has been a growing interest in potential applications in nanoelectronics of TMD materials due to their highly tunnable properties. Part of their tunnability appear from the 2D confinement of the materials into the monolayer regime. The very promising properties of TMDs encouraged an intense investigation of their optical and mechanical properties by different techniques.

This chapter is an introduction to the experimental techniques used to investigate different properties of TMD materials, together with the sample preparation procedure. The weak interlayer interactions of TMDs enable the mechanical exfoliation of single layers. The TMD flakes are then stamped on different substrates.

The optical and electrical characterization of the different materials and the devices is performed mostly with a confocal microscope. This microscope is equipped with a digital multimeter for electrical measurements and a spectrometer for the optical characterization. The spectrometer has different grids and a CCD detector with very low signal to noise ratio. Moreover, it is possible to add different optical components to the detection and emission path in order to perform a polarization characterization.

Confocal microscope are diffraction limitted, so to increase the spatial resolution for the optoelectronic characterization the devices are studied by near field optics using a s-SNOM. The microscope was equipped with an inelastically scattered light detector, spectrometer and CCD detector, to detect the optical and electrical signal quasi-simultaneously (TERS-s-SNOM setup).

2.1 Sample preparation

2D materials and more specifically TMDs are characterized by their strong intralayer and weak interlayer interactions, enabling a layer by layer separation by mechanical exfoliation. The exfoliation occurs along the crystallographic planes breaking the layer-to-layer bonds. Hence, this is a widely used technique to prepare samples with single-layer flakes.

In this thesis, we aimed to produce single-layer and heterostructure devices. The number of steps needed to obtain monolayers differs from one material to the other depending for example on the cohesive force between the layers. All the steps were performed with a setup and the knowledge developed in the nanodevices group at CIC nanoGUNE, which is shown in figure 2.1.

The bulk crystal is exfoliated using a scotch-type tape (blue tape). The first exfoliation cleans the crystal, removing possible oxide layers. The other blue tapes are re-exfoliated several times to obtain the optimum quantity of material. We found that this step is the limiting step for later obtaining larger monolayer flakes.

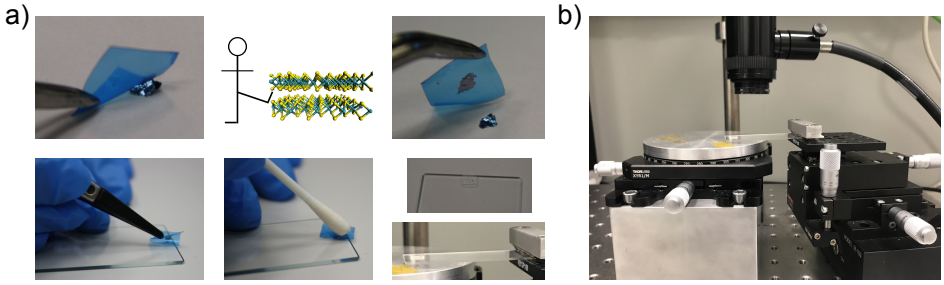

Figure 2.1: a) Exfoliation process. The crystal is exfoliated with a blue tape, separating the material by layers. The blue tape can be place on a PDMS place on the microscope slide and later stamp it. b) Stamping setup developed by the nanodecices group in CIC nanoGUNE.

Then, there are two possible methods for stamping the clean flake on the substrate: to place the tape directly on the substrate or to re-exfoliate the blue tape with a polydimethylsiloxane (PDMS) placed on transparent microscope slide (Figure 2.1). The fastest method is to place the material directly on the substrate. However, in this way we lose the control on the stamping position and on the number of layers. Therefore, this method used only to obtain thick flakes of $NbSe_2$. The second method is more controlled, allowing to select a flake with a specific number of layers and select the place where it will be stamped. Therefore, we used this method

to obtain monolayer flakes of MoS_2 and WSe_2.

Monolayers of MoS_2 and WSe_2 on the PDMS can be identified with an optical microscope. They are almost transparent in transmission mode, but in reflection mode can be observed. Furthermore, the number of layers can be confirmed via photoluminescence and Raman spectroscopy before the stamping step (see section 3.2). Then the single-layer flakes are stamped on different substrates (SiO_2 and YIG) or on top of other materials ($NbSe_2$) to create heterostructures using a positioning stage and optical access.

Some of the materials studied in the thesis, specially $NbSe_2$, get easily oxidized after being in contact with air for few minutes. The oxidation is expected to appear only in the upper-most layers. Hence, the heterostructure devices used in chapter 4 have a rather thick (50 nm) $NbSe_2$ flake. Then, the 1L-MoS_2 flake is stamped on top creating a vertical heterostructure. Even that this second process is done as fast as possible after the exfoliation of $NbSe_2$, a small barrier is assumed to exist in the contact area between the two materials. Shortly after, the sample is covered by the lithography resist (PMMA-polymethyl methacrylate) protecting the full sample from oxidation.

The covering of the sample with PMMA includes two spinning steps to place the resists used for the lithography (PMMA resist covering: 1. PMMA (495 A4) 4000 rpm for 1 min 2. PMMA (950 A2) 4000 rpm for 1 min, bake after each spinning step at 180° for 90 seconds). The two steps are able to damage the sample due to the weak adhesion of MoS_2 to SiO_2 or to $NbSe_2$. Afterwards, the sample is patterned by electron beam lithography (EBL) and developed with 1:3 MIBK:IPA (methyl isobutyl ketone:isopropanol) for 60 seconds. The e-beam interacts with the PMMA, so the developer leave the patterned areas exposed.

Later, the sample is fully covered with the contacting metal by evaporating 5 nm of titanium (Ti) or chromium (Cr) and 50 nm of gold (Au). The Ti and Cr are used as adhesive layers, since Au does not easily stick to the materials when is evaporated. The final step consists on an overnight lift-off in acetone, removing the extra deposited metal over the unpatterned PMMA region. For the heterostructure devices the samples were longer in acetone to avoid the usage of the ultrasound bath and still ensure a total lift-off. (Special acknowledgment to Saül Vélez and Juan Manuel Gómez).

2.2 Confocal microscopy

The optical and electrical properties of materials can be studied through optical spectroscopy, based on the study of the interaction of matter and light, originally visible light. Nowadays, optical spectroscopy has improved and

includes the study of the interaction between matter and light along a larger area of the electromagnetic spectrum (ultraviolet, infrared, microwaves or terahertz). Moreover, the appearance of light microscopy and the later improvement with confocal microscopy, revolutionized the field by increasing the resolution and capability of the technique.

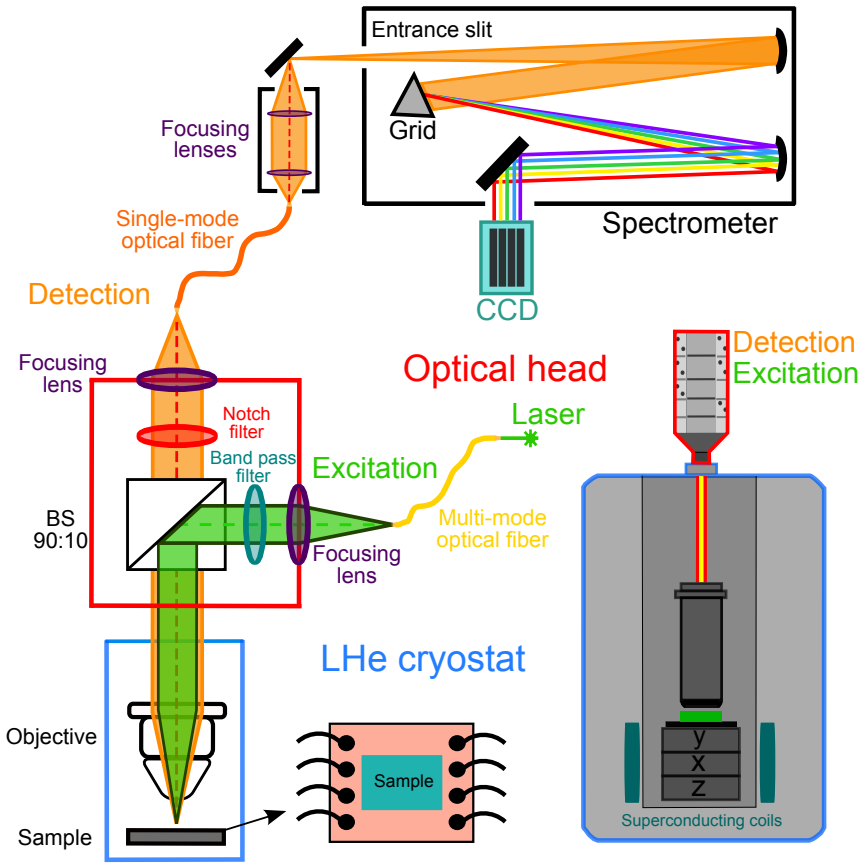

Figure 2.2: Confocal microscope setup in the Attocube low temperature system. The LHe cryostat (in blue) contains the superconducting coil, the sample on top of x-y-z positioners and the objective that focuses the excitation and collect the scattered light. The optical head (red) can hold filters, polarizers or wave retarders. The spectrometer (black) disperses the signal and the spectrum is recorded by the a charge-coupled-device, CCD camera (turquoise).

For the development of this thesis I used two commercial confocal microscopes one from Witec with the optical spectroscopy implemented (Witec alpha 300) and an Attocube microscope only with confocal access (attoCFM

I). The attoCFM is a multi-functional microscope that can be use as a confocal microscope or as an atomic force microscope (AFM) by exchanging the lens by a head with a cantilever and detecting the signal with an optical interferometer detector.

The Attocube microscope works at variable temperatures from room temperature to a minimum of 2 K. In addition, three superconducting solenoids can apply a vector magnetic field of 5 T in z-axis and 1 in X-Y-axis. The solenoids are at the bottom of the LHe cryostat where the microscope stick is inserted and on top of all is placed an optical head (Figure 2.2). During the thesis, we updated this versatile setup to additionally perform spectroscopic analysis, by coupling it with a confocal optical setup [56–58] described in figure 2.2.

The light from a monochromatic laser is driven to the optical head through a multi-mode FC/APC optical fiber (MM) and the detection is introduced into the spectrometer by a single-mode FC/APC optical fiber (SM). The usage of optical fibers simplifies the alignment procedure at LT when there is no visual access to the optical path. In order to analyze the inelastically scattered light the sample has to be excited with a monochromatic excitation. The excitation beam passes through a band pass filter before the beam splitter (90:10 for most of the experiments to maximized the transmission, emitted light) and is guided as a free collimated beam into the low temperature inset towards the objective. The Attocube microscope has such a long optical path (2 m optical path) that the collimation is a limiting aspect in the intensity detection limit.

The objective focuses the light into the focal point and collect both the Rayleigh and the inelastically backscattered light. The objective is a high numerical aperture apochromatic objective (NA = 0.82), with a 654 nm spot size, 463 nm confocal resolution in the visible and a magnification of 50. The optimum working spectral range is from 400 to 700 nm and it has a optimum working distance of 0.65 mm. The sample sits on top of a stack of x-y-z positioners and a scanner for image acquisition and has 8 electric contacts. The contacts are used to characterize the electronic properties of the devices with a digital multimeter (Keithley's Series 2600B System SMU).

The backscattered light from the sample is collected and collimated by the objective. In the optical head, a notch filter suppresses the elastically scattered light before the inelastic light is driven by an optical fiber (multimode fiber) into the spectrometer. The grating inside the spectrometer (Acton SP2500i, Princeton instruments, gratings: 300, 600 and 1200 points) disperses the spectrum emitted by the sample (Raman or photoluminescence). The spectrum is then recorded by a charge-coupled-device (CCD) camera (iXON ultra, ANDOR Si CCD camera with 1024 x 1024 pixels).

In addition to the filters placed in the optical head, which allow the spectroscopic characterization of the materials, other optical components such polarizers or wave retarders can be added. This enables the selective excitation and detection with linearly and circularly polarized light in different directions, as discuss in a later section.

2.2.1 Programing in LabVIEW

The setup described in the previous section has three different equipments. For the optical detection we need the spectrophotometer and the CCD, the digital multimeter for the electrical characterization and the microscope electronics for scanning through the device. The communication among them and the saving of the acquired data is programed by Labview.

LabVIEW is a National Instrument software that allows to combine the data acquisition with different hardwares and the data saving, all by graphical programming. The program also allows the user to represent graphically the data and to analyze it. However, during this thesis all the effort was focused on the communication and data acquisition role. The program was implemented in a way that enabled to use it in the two microscopes used during the thesis (Attocube and Wittec).

The optical characterization (point spectra measurements) were done with the commercial software provided by the company of the CCD. For the electrical measurements the developed LabVIEW program is mainly used to perform current-voltage curves. The voltage is ramped while the current is measured. In this program it is also possible to perform 2D sweeps, V_{sd} and V_g ramp while measuring the current.

For mapping the device, the LabVIEW program uses as a base a scanning grid option from each microscope (Attocube and Wittec). The scanning grid is determined by a the number of pixels of the map, the size of the map and the acquisition time. When the microscope reaches one of the pixels it sends an order to the spectrometer and the multimeter. Then both equipments measure simultaneously the optical and the electrical signal (photoluminescence and current) and send the order to the microscope to move to the next pixel. This is repeated over the grid creating two XY 2D arrays with the light and current intensity on each point.

Moreover, it is possible to obtain XY 3D arrays performing at each pixel a photoluminescence spectrum or a current-voltage sweep. Finally, I would like to thank Oscar Val that started one of the LabVIEW programs and Reyes Calvo for the help.

2.2.2 Polarized light setup

Optical properties can be generally tunned by either linearly or circularly polarized light in most of the materials. More specifically in TMDs, polarized light enables the accesses to a new degree of freedom, the valley pseudo-spin, increasing the number of possible applications for TMDs. The goal of the polarized light setup is mainly to excite and detect linearly and circularly polarized light, to access this degree of freedom .

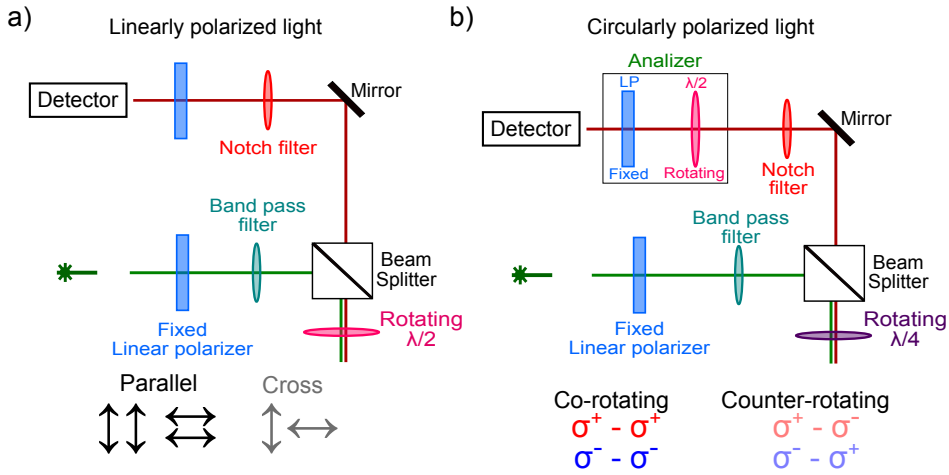

Figure 2.3: a) Linearly polarized light setup, fixed linear polarizer (LP) in both excitation and detection paths and rotating $\lambda/2$ wave plate between the beam splitter and objective. Parallel and cross linear polarization detection. b) Circularly polarized light setup, fixed LP in the excitation path, rotating $\lambda/4$ wave plate between the beam splitter and objective, and analyzer in the detection path (fixed LP and rotating $\lambda/2$ wave plate). Co- and counter-rotating detection for left- and right-handed circularly polarized light.

The linear polarization of the excitation green laser is not 100% maintained by the optical fibers and thus a fixed linear polarizer before the beam splitter filters the direction of linearly polarized light (horizontal direction). Similarly, the polarization direction of the detection is fixed to the maximum intensity of the spectrometer (horizontal direction).

For linearly polarized light experiments, a rotating $\lambda/2$ wave plate is placed between the beam splitter and the objective as it is shown in figure 2.3-a. This allows turning the direction of the excitation and detection polarization in the same direction. This way the detection is always done in a parallel configuration. For experiments in which we measure the cross detection, the rotating $\lambda/2$ wave plate is placed right before the linear polarizer fixed in the detection.

For experiments with circularly polarized light (Figure 2.3-b), the rotating $\lambda/2$ wave plate is kept at the detection and a wave retarded, $\lambda/4$ wave plate, is placed before the objective. Linearly polarized light reaches the rotating $\lambda/4$ wave plate that retards the electromagnetic wavefront creating left and right circularly polarized light. Then the backscattered circularly polarized light from the sample passes through the $\lambda/4$ wave plate getting back to linear polarization. The emission with left-handed polarization is turned into a linearly polarized light with the wavefront in the horizontal direction. Contrary, the circularly polarized scattered light in the right-handed direction will be turn in a linearly polarized light in the vertical direction.

Finally, the $\lambda/2$ wave plate located in the analyzer, turns the linear polarization to fit the direction of the fixed linear polarizer. The rotation of the $\lambda/2$ and the $\lambda/4$ wave plates allows the combined excitation and detection of different polarizations (Table 2.1).

	$\lambda/4$ wave plate	$\lambda/2$ wave plate
Parallel ($I_{\parallel}$)	No	0°
Parallel ($I_{=}$)	No	45°
Co-rotating left ($I_{(\sigma_+-\sigma_+)}$)	45°	0°
Co-rotating right ($I_{(\sigma_--\sigma_-)}$)	-45°	0°
Counter-rotating left ($I_{(\sigma_+-\sigma_-)}$)	45°	45°
Counter-rotating right ($I_{(\sigma_--\sigma_+)}$)	-45°	45°

Table 2.1: $\lambda/2$ and $\lambda/4$ wave plates angles to obtain linearly polarized excitation and parallel and cross detection and co- and counter rotating detection for left- and right-handed circularly polarized excitation.

The first and most important step of the setup alignement, is to determine the polarization axis of the excitation light. This characterization is done using Si wafers with different crystallographic orientations. The intensity of the main Raman mode changes with the orientation of linearly polarized light for Si (100), while stays invariant for Si (111) (Figure 2.4-b, peak at 500 cm^{-1}). Thus, the Raman spectrum of Si is measured while turning the $\lambda/2$ wave plate in the microscope stick. This ensures the parallel detection, while the polarization direction is turned over the sample.

The polar plot of the Si Raman mode intensity in figure 2.4 as a function of the $\lambda/2$ wave plate angle shows a maximum-minimum, cross-like shape for Si (100) and circular shape for Si (111). The different shapes of the polar plots are the characteristic dependences of the Si Raman mode in linear polarization basis.

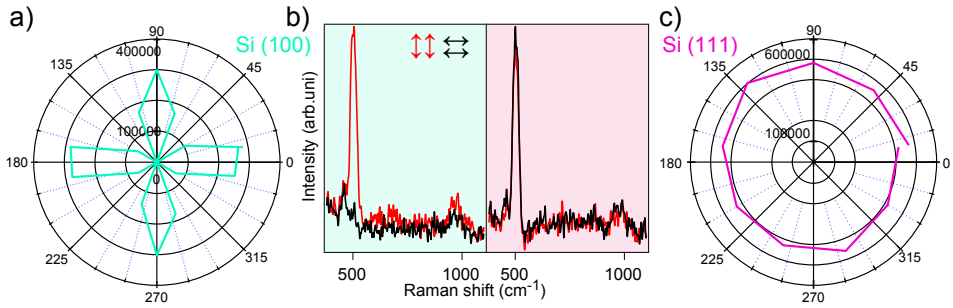

Figure 2.4: a) Polar plot of the Si (100) Raman mode (peak at 500 cm^{-1}) for different detection angles. b) Raman spectra of Si (100) (left) and of Si (111) (right). c) Polar plot of the Si (111) Raman mode (peak at 500 cm^{-1}) for different detection angles.

The last step of the alignment consists on moving the $\lambda/2$ wave plate to the detection path and adding the $\lambda/4$ wave plate before the objective. The measurements on Si 100 and 111 are repeated, showing the same dependence when the $\lambda/4$ wave plate is kept at 0°, linear polarization does not change when passing by the circular polarizer. Additionally, circular polarization can be characterized by using chiral molecules such CCl_4 (tetrachloromethane), having in mind the high toxicity of the substance. I specially thank Patryk Kusch and Stephanie Reig for the help while mounting the setup.

2.3 Combined TEPC/TEPL and a near-field optics (TEPC-TEPL-s-SNOM)

The spatial resolution in confocal microscopes is diffraction limited due to the diffraction of the propagating light. The resolution is typically obtained as $NA^*\lambda$ (NA: numerical aperture of the objective; λ: excitation wavelength) and the maximum resolution achievable with these microscopes can be approximated to $\lambda/2$, the Abbe limit. However, there are other imaging techniques capable to beat the diffraction limit, the scanning probe microscopies (SPM). An example of these microscopes are the Scanning Tunneling Microscope (STM), the Atomic Force Microscope (AFM) or the Magnetic Force Microscope (MFM). The SPM image is created by a sharp probe (tip) scanned along the sample and the resolution is given by the size of the tip apex (10-20 nm for commercially available tips).

The combination of the SPM techniques with the spectroscopic analy-

sis (optical and electrical) is a very powerful technique able to overcome the diffraction limit of conventional microscopes. Tip-enhanced Raman Spectroscopy (TERS), Tip-enhanced Photoluminescence (TEPL) and Tip-enhanced Photocurrent (TEPC) are a derivation from surface-enhanced Raman spectroscopy (SERS) where the tip focuses light generating an enhancement of the point Raman scattered signal. Typically, the TERS-TEPL-TEPC signals are collected from an area of tens of nanometers bellow the tip corresponding to the size of the concentration of the electromagnetic field to a near-field spot at the tip-apex [24].

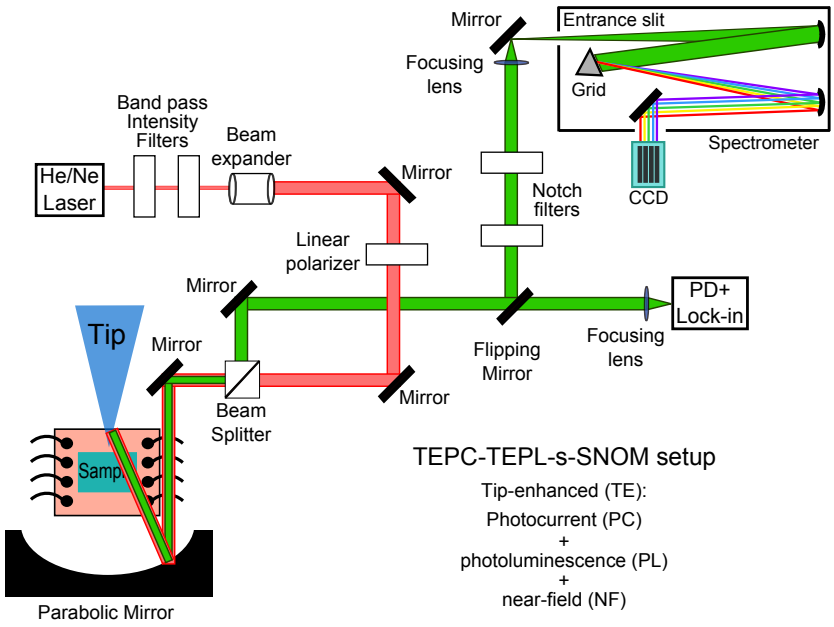

Figure 2.5: Combined setup: Tip-enhanced Photocurrent (TEPC), Tip-enhanced Photoluminescence/Raman spectroscopy (TEPL-TERS), scattering-type Scanning Near-field Optical microscopy (s-SNOM). TERS-s-SNOM setup. [24]

Scanning Near-field Optical Microscopy (SNOM) studies tip-sample interactions in order to create an optical image of the sample. We use a commercial s-SNOM (NeaSNOM from Neaspec GmbH, Germany), that uses an AFM in tapping mode. The tip is mounted on a flexible cantilever and the bending caused by the tip-sample interactions is monitored by a reflecting laser and an interferometer detector.

The sharp metallic tip of the AFM is illuminated by visible light (He-Ne laser-1.9 eV). The laser light passes through a band pass filter, power filters and a linear polarizer before is guided by a beam expander to a parabolic

mirror that focuses the light in the AFM tip and collects the backscattered signal (Figure 2.5). This signal is then analyzed by a photo-detector with a lock-in or by the spectrometer, selected by the flip mirror.

The modulation of the tip-sample separation allows the effective suppression of the background by selecting the 3rd harmonic of the demodulated backscattered signal from the tip. In order to correlate the spectroscopic response (photoluminescence and Raman spectroscopy) and the optoelectronic properties of TMDs with a resolution bellow the diffraction limit, we equipped the s-SNOM with a single grating Raman spectrometer (Acton SP2500i, Princeton instruments), coupled to a silicon charge-coupled-device (iXON ultra, ANDOR Si CCD camera with 1024 x 1024 pixels). Moreover, the sample sits on a sample holder with electric contacts for photocurrent measurements analyzing the signal with a lock-in amplifier.

With this combined microscope it is possible to simultaneously obtain the topography, the near-field signal, the photocurrent and the Raman or photoluminescence signal.The resolution in this case is determined by the tip apex (10-20 nm for commercially available tips) and not by the illumination wavelength. I would like to specially thank Stefan Master and Rainer Hillenbrand for all the near-field optics discussions, Patryk Kusch involved in the setup preparation and CIC09 (nanoimaging group) members for AFM discussions.

Chapter 3

Optical Characterization of TMDs

The optical properties of TMDs change with the number of layers, hence we can characterize the number of layers by Raman spectroscopy and photoluminescence. Raman spectroscopy is a very extended technique to determine the number of layers and the purity without damaging the material.

The photoluminescence intensity and energy also change with the number of layers due to a change in the band structure of TMDs. Additionally, the photoluminescence peaks are narrower at low temperature, allowing the identification of different resonances.

The characterization by Raman active modes and the photoluminescence or emission, is performed for the three different materials that we used for the measurement: MoS_2, WSe_2 and $NbSe_2$. All the optical characterization showed in this chapter is performed in a confocal microscope. The microscope is equipped with a spectrophotometer with a CCD camera.

3.1 Photoluminescence

The main characteristic that differentiates semiconductors from metals is the appearance of an energy gap (E_g) between hundreds of meV and few eV. In principle, inside the gap there are no available states, whereas inside the bands there is a continuum of energy levels. Similar to the HOMO/LUMO levels in a molecule, semiconductor materials has a fully occupied band, the valence band (VB) and an unoccupied band, the conduction band (CB).

The absorption of certain electromagnetic radiation, can excite an electron from the VB to the CB, leaving a positively charged, hole, in the VB. The electron in the CB and the hole in the VB are attracted by Coulomb interactions forming a quasi-particle known as "exciton". The later recombination of the e-h pair has a certain probability of emitting a photon, producing the photoluminescence (PL) radiation. The efficiency is determined by the excitation and recombination process and by the selection rules.

Excitation process: In any spectroscopy measurement, the photoexcitation can be done with a resonant, quasi-resonant or non-resonant energy. In a resonant excitation situation, the excitation energy is similar to the emission energy ($\lambda_{exc} = E_g$), making more challenging to distinguishing between the Rayleigh radiation and the inelastic emission. To overcome this problem, in the quasi-resonant case, the excitation energy is slightly higher than the transition energy. Finally, in non-resonant excitation experiments, the electrons in the VB are excited with an energy higher than the gap energy. In this thesis, I explore the photoluminescence response mostly after a non-resonant excitation, using a green laser (532 nm, 2.33 eV).

Recombination process: The recombination of the electron-hole pair can follow radiative or non-radiative paths depending if the electron interacts with other electrons, holes or vibrational states. The non-radiative path, for example occurs when the recombination has a certain momentum mismatch. The recombination can be assisted by impurities of the lattice, which create mid-gap or localized states. Contrary to non-radiative recombination, when the excited electron can recombine without any momentum change, it emits a photon with an energy corresponding to the band gap of the semiconductor. This recombination process occurs mainly in direct-gap semiconductors for which the VB and CB have the same momentum energy at the band maxim or minim.

Selection rules in photoluminescence: Electronic transitions are governed by two selection rules: spin and parity. The spin section rule forbids any electronic transition implying levels with a different spin states (i.e. $\Delta S \neq 0$) because of spi-momentum conservation. For materials with small spin-orbit coupling this selection rule is strict. However, in materials with a strong spin-orbit coupling, such as TMDs, this selection rule is not

determinant because of a mixing of different spin states.

The parity selection rules forbids any electronic transition from states with the same parity, because the absorption of a photon through electric dipole transitions, requires a charge of the electric dipole in the transition state between ground state and excited state. In transitions between states with the same parity there is no dipolar change, so these transitions are forbidden by this selection rule.

Charge excitons: In some semiconductors the presence of extra negative or positive charge carriers, induces the formation of trions. Trions are charged excitons formed by two electrons and a hole (T^-) or by one electron and two holes (T^+). In principle, both T^- and T^+ should have the same energy and their intensity should only depend on the available extra charges typically tunned by a back gate voltage [59–61].

3.1.1 Photoluminescence of semiconducting TMDs

In bulk TMDs such MoS_2 or WSe_2, the direct transition at K point has higher energies than the indirect, phonon-mediated transition [20–22]. The reduction in the number of layers induces an increment of the energy of indirect transition favoring an exciton recombination at the K point (Figure 3.1-a). The direct recombinations are also favored by selection rules, angular momentum conservation transitions. Thus, in the single-layer limit the less energetic direct recombination occurs with more probability than the indirect recombination. The change in the type of gap and the renormalization of the gap when reducing the number of layers of both studied materials, MoS_2 and WSe_2, increases the photoluminescence quantum efficiency (QE) and modifies the energy of the transition. The indirect- to direct-gap transitions is one of the most interesting and tunable properties of these materials, increasing the interest for possible opto-electronic applications.

The strong spin orbit coupling in these materials produces a splitting of the bands. The spin-orbit splitting (SOS, Δ_{SO}) is on the order of 30 to 40 meV, and is negative for W-based materials and positive for Mo-based materials. For WX_2 the lowest energy transition does not preserve spin, thus is not optically active and is called "dark exciton" (Figure 3.1-b). The optically active exciton (bright exciton) in WX_2 materials is generated by the recombination of an electron in the upper-splitted level of the conduction band with a hole from the valence band. Since Δ_{SO} is positive for MoX_2 materials, the bright exciton corresponds to the lowest energy transition [23]. This specific ordering of the bright and dark excitons lead to the growth of photoluminescence intensity with temperature for W-based materials and the decrease for Mo-based ones.

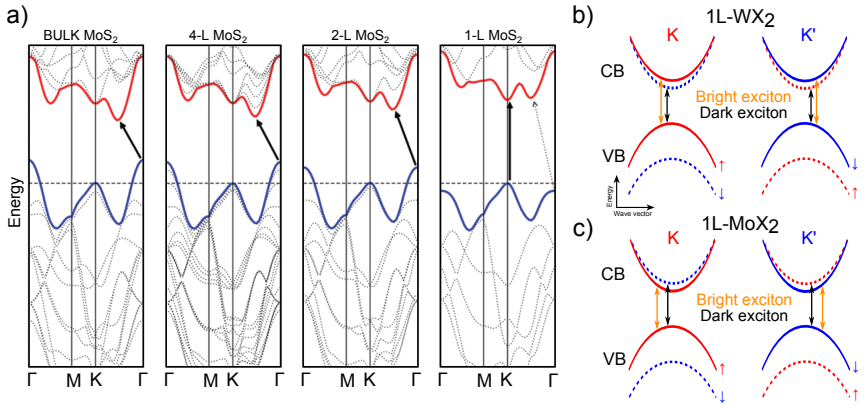

Figure 3.1: a) Calculated band structures of bulk, 4-L, 2-L and 1-L of MoS_2. The solid arrows indicate the lowest energy transitions. Figure adapted from [22]. b-c) Schematic picture of the conduction and valence band splitting in K and K′ points for b) Mo- and b) W-based TMDs.

Photoluminescence spectrum for different number of layers: At room temperature WSe_2 has a large QE what allows to measure the emission of flakes with large number of layers, observing an energy shift from 1.57 to 1.66 eV when decreasing the number of layers (Figure 3.2-a). However, for MoS_2 the photoluminescence drastically drops when increasing the number of layers, thus it is not possible to observe the predicted shift of 1.2 to 1.9 eV from bulk to single layer, observing only a shift from 1.84 eV (1L) to 1.86 eV (multilayer) (Figure 3.2-b).

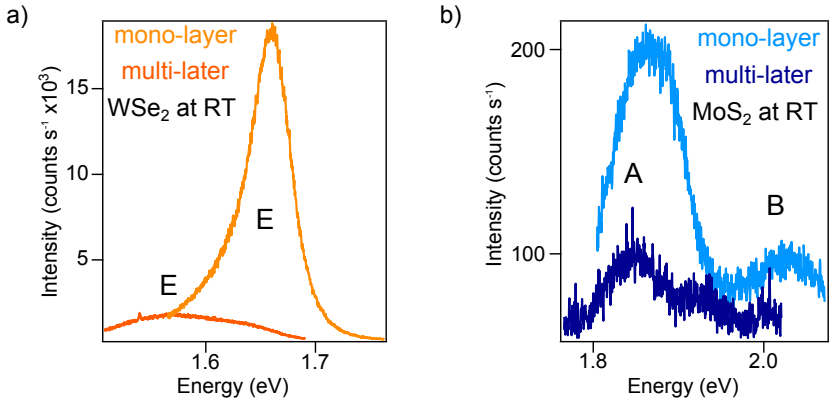

Figure 3.2: Photoluminescence spectra at room temperature after green excitation of: a) 1 layer and multilayer WSe_2 b) 1 layer and multilayer MoS_2. The spectra are normalized to the acquisition exposure time ($counts\ s^{-1}$).

Temperature dependence of photoluminescence spectrum: Temperature also affects the photoluminescence intensity due to thermal activated processes. The parity selection rule excludes radiative recombinations when the electron and the hole have different spin orientation. The selection rules together with the spin splitting of the bands and the polarization for each valley result in a certain number of allowed transitions for MoX_2 and WX_2 and other that are forbidden (dark). The combination of photoluminescence selection rules and the band structure of W- or Mo-base TMDs, makes that for WSe_2 the intensity is larger at RT contrary to MoS_2 where the intensity increases when lowering the temperature to 77 K (Figure 3.3). The temperature dependence is a consequence of the larger thermal energy required to overcome the localization potential in WX_2 [62–64].

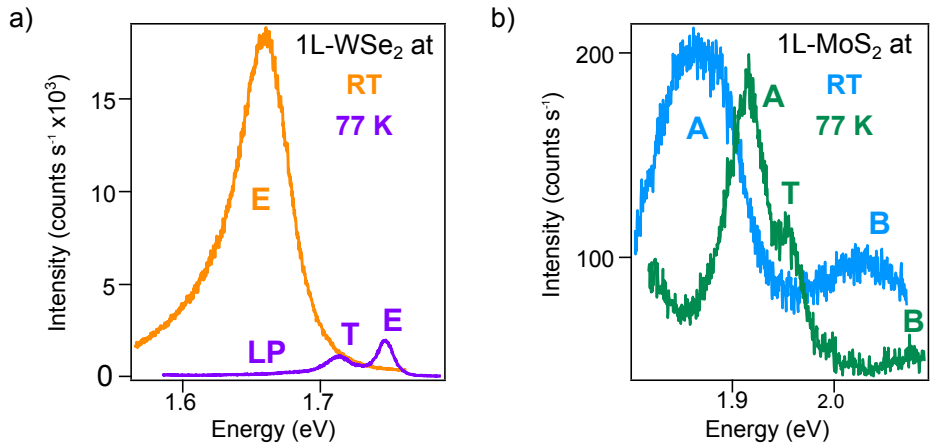

Figure 3.3: Photoluminescence spectra after green excitation of: a) 1L-WSe_2 at room temperature and 77 K b) 1L-MoS_2 at room temperature and 77 K. The spectra are normalized to the acquisition exposure time ($counts\ s^{-1}$).

For WSe_2 (Figure 3.3-a), a dark material, the photoluminescence spectrum has higher intensity at high temperatures. The photoluminescence spectrum at room temperature has a broad peak corresponding to the exciton (E). However, at 77 K the spectrum has narrower peaks, enabling the identification of the exciton (E), trion (T) and several peaks corresponding to localized states (LP). Due to the large SOS in WSe_2 it is only possible to observe one of the exciton resonances.

MoS_2 is a bright material so the photoluminescence intensity increases when lowering the temperature (Figure 3.3-b). For this material the SOS is smaller so at room temperature the spectrum has two broad peaks corresponding to the A and B exciton resonances. At 77 K the intensity of the spectrum does not increase but the peaks are narrower. The A exciton

peak splits in two that are assigned to the a exciton and the corresponding trion.

For both materials, we see a shift in energy when lowering the temperature. To measure from room temperature down to 4 K the 1L-WSe_2 flake on a SiO_2 substrate is mounted in a variable temperature insert (VTI) in a liquid helium (LHe) cryostat (Experimental setup in 2.2). In figure 3.4-a we present the evolution of 1L-WSe_2 photoluminescence spectrum with temperature.

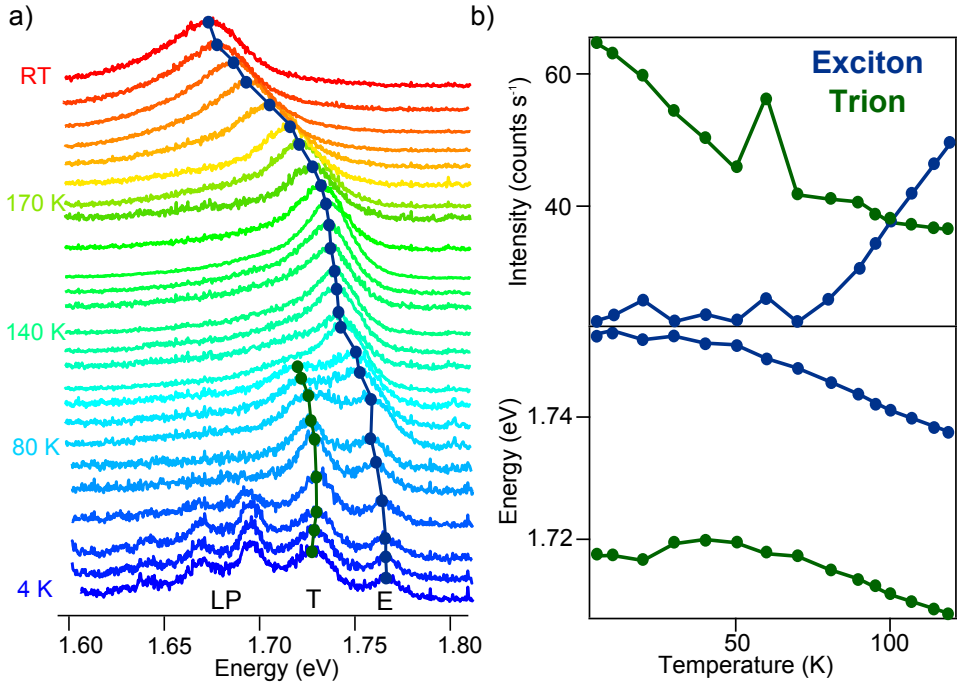

Figure 3.4: a) Photoluminescence spectrum evolution with temperature (RT to 4 K) of 1L-WSe_2 after green laser excitation. b) Temperature evolution of the intensity and energy of the exciton (blue) and trion (green)

The intensity of the exciton (blue line in figure 3.4-b) increases with temperature corresponding to the increment of thermal activation needed to have bright excitons in WSe_2. However, the trion (green line) decreases until it merges with the exciton peak, due to the resolution lost with temperature. The energy of both exciton and trion stays almost invariant for low temperatures, but at temperatures higher than 170 K the exciton redshifts, due to thermal stabilization processes [65–68].

3.1.2 Photoluminescence of MoS_2 heterostructures

In this section, the spatial distribution of the exciton intensity and energy is optically characterized for MoS_2 and $NbSe_2$ -MoS_2 heterostructures by photoluminescence microscopy. The optoelectronic processes include the breaking of an electron-hole pair, so the generation of photocurrent is expected to affect the recombinarion and hence the photoluminescence QE. Also the change of photoluminescence intensity with the number of layer due to the indirect- to direct-gap transition can be used to determine the number of layers. However, Raman spectroscopy is a much more efficient technique to determine the number of layers.

Photoluminescence maps of MoS_2 isotype heterostructures: We record the photoluminescence spectrum at different points over the red square in figure 3.5-a. In figure 3.5-b the photoluminescence intensity is integrated over the A exciton energy range. The change of the gap type when decreasing the number of layers is observed as an increment of the photoluminescence QE, thus the 1L area has higher intensity (brighter area) than to the 3L area (darker area).

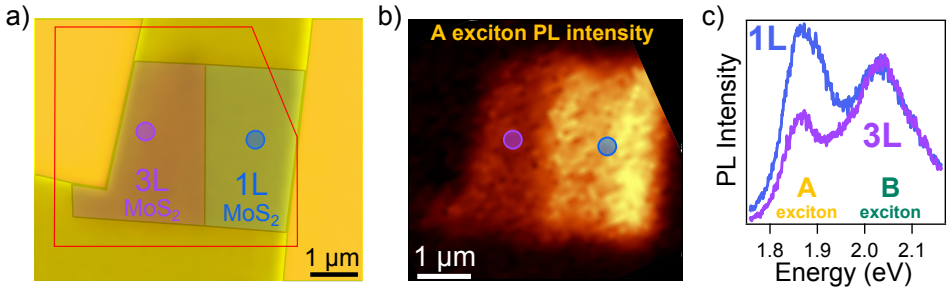

Figure 3.5: a) Optical microscope image of the 1L/3L-MoS_2 heterostructure device. b) Photoluminescence intensity map integrated over the A exciton, yellow area. c) Photoluminescence spectrum of 3L- and 1L-MoS_2.

The interaction between the MoS_2 flake and the substrate creates perturbations such as local gating or strain [69–71]. The roughness-induced strain is responsible for the inhomogeneous distribution of the exciton emission on both 1L and 3L areas. In Si substrates with 250 nm of SiO_2, the roughness is around 190 pm as measured by AFM [72, 73]. The strain induced by the substrate modifies the intensity and energy of the resonances giving the inhomogeneous distribution of intensity along the flake (Figure 3.5).

Photoluminescence quenching in MoS_2-$NbSe_2$ heterostructures: The other heterostructures measured in this thesis are made of 1L-MoS_2 flake on top of a thick $NbSe_2$ flake, with SiO_2 as substrate.

In figure 3.6 the photoluminescence spectra are acquired at different positions of the heterostructure. The $NbSe_2$ flake has areas with different number of layers what enables to study the evolution of the emission with the number of layers. Generally, metals produce a broad emission in the visible [74]. Thus, the spectrum of $NbSe_2$ is characterized by a broad peak. The intensity of the spectrum increases with the number of layers (70 layer, 20 layers and 10 layers).

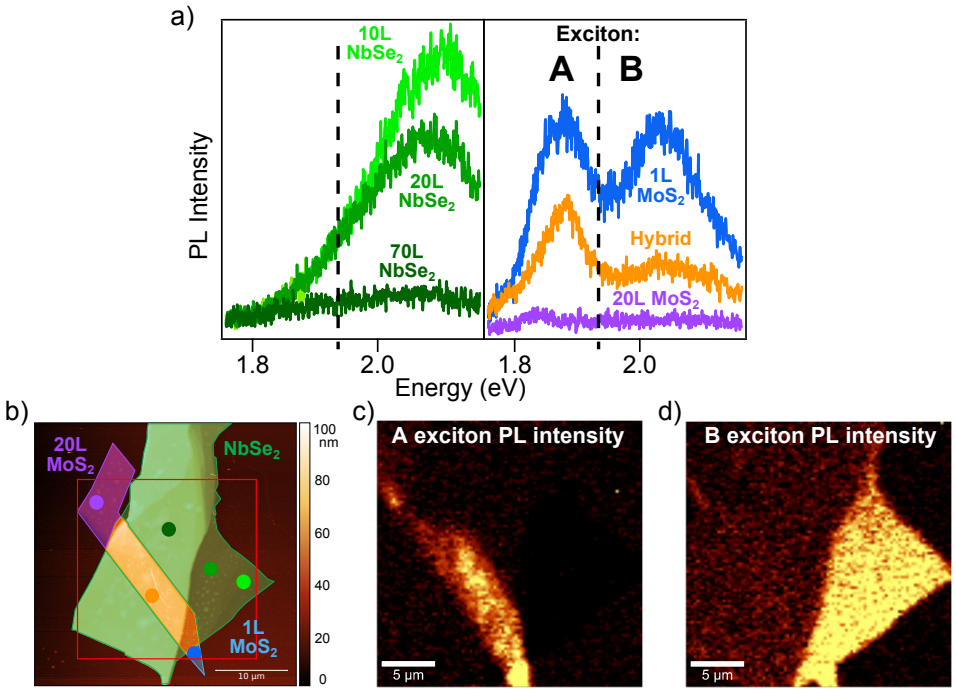

Figure 3.6: a) Photoluminescence spectra of the heterostructure acquired on 70L-, 20L- and 10L-$NbSe_2$, 1L-MoS_2, 20L-MoS_2 and on the $MoS_2/NbSe_2$ heterostructure. Each color corresponds to a certain position in the AFM image. b) AFM image of a 1L-$MoS_2/NbSe_2$ heterostructure. c) Photoluminescence intensity map integrating over the A exciton (from 1.75 to 1.95 eV). d) Photoluminescence intensity map integrating over the B exciton (from 1.95 to 2.16 eV).

In the photoluminescence spectrum of 1L-MoS_2, the two peaks correspond to the photoluminescence from the A and B exciton. The photoluminescence of MoS_2 almost disappears for 20 layers of the material as a consequence of the change in the gap type (bulk MoS_2 has an indirect gap). The orange spectrum, acquired on the heterostructure, presents the quenching of the MoS_2 photoluminescence. The quenching of photolumi-

nescence from semiconductors in contact with metals is generally associated with resonance energy transfer phenomenas [74–78].

The photoluminescence map of the heterostructure demonstrate the quenching of the MoS_2 photoluminescence. The quenching of the A exciton at the hybrid is clear in panel c, where the intensity is higher at the 1L, decreases at the heterostructure and disappears at the area of 20 layers. The intensity map of the B exciton, shows a high intensity area at the 10 to 20 layers of $NbSe_2$ and at the 1L-MoS_2 on SiO_2 due to the emission band of $NbSe_2$ and the B exciton of MoS_2 (Figure 3.6-d). The emission spectrum of $NbSe_2$ has a broad peak at around 2.1 eV that changes with the number of layers so the intensity on the thick area (70 layers) of $NbSe_2$ is bellow the noise signal.

It has been shown that, photoluminescence is a highly valuable spectroscopic technique to investigate the electron-hole interactions that will play a role in the photocurrent generation at the devices studied in this thesis.

3.2 Raman Spectroscopy

Raman spectroscopy is a technique that studies the inelastic interaction of radiation and matter, implying a change on the excitation light frequency, the Raman shift. Raman spectroscopy, measures the amount of inelastically backscattered light for a certain wavelength and polarization angles, giving information about the characteristic vibrational, rotational and different low-frequency modes that are fingerprints in each material.

The system is excited by a laser source with a frequency ν_0, taking the system into an excited virtual state from which it decays emitting elastic Rayleigh radiation (ν_0), Raman-Stokes (ν_0-ν_{ml}) and Raman-antiStokes (ν_0+ν_{ml}) (Figure 3.7). Both the Raman-Stokes and the anti-Stokes are produced as a result of the interaction of the inelastic scattered photon with different excitations from the system, so the energy lost during the scattering is equivalent to the energy given to the molecular vibrations. Thus, any variation of electronic properties due to defects, doping or magnetic fields, affects positions, widths, and intensity of Raman peaks.

The probability of producing Stokes or Anti-Stokes signals is about 0.001% of the incident light, what makes the Raman processes very unlikely to occur increasing the importance of a very accurately aligned setup. Also, since the population of the excited states is commonly much lower than for the fundamental state, the Raman Stokes dispersion is more intense than the anti-Stokes. Experimentally the very efficient Rayleigh scattering is filtered out with an edge or notch filter, avoiding the damage of the detector (for details about the setup see section 2.2). Also, if the system has an

energy level that matches the energy of the excitation, real state instead of virtual states, the process became resonant, increasing the efficiency of the Raman signal.

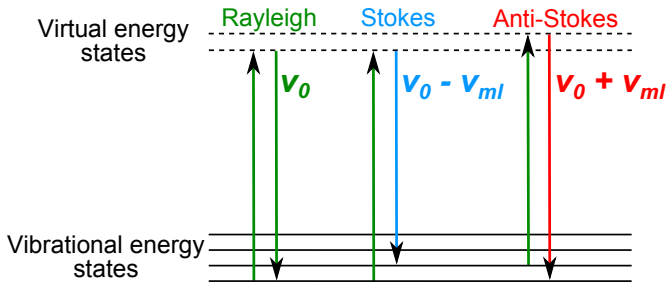

Figure 3.7: Raman spectroscopy energy levels mechanism.

Selection rules: The activation of vibrational modes in Raman spectroscopy is triggered by the selections rules, the mutual exclusion principle and the change of polarizability. The mutual exclusion principle ban the Raman active modes from being IR active. Vibrational modes become Raman active when the polarizability of the material (α, that measures the deformability of a bond in the presence of an electric field) changes with the coordinate q of the vibrational displacement ($(\frac{d\alpha}{dq}) \neq 0$).

3.2.1 Raman spectroscopy of semiconducting TMDs

Raman spectroscopy is a very convenient technique to characterize the number of layers in TMDs due to the variation that both the intensity and energy of the modes has with the number of layers or the presence of defects. Here the Raman signal of MoS_2 and WSe_2 is measured to identify the number of layers.

MoS_2 Raman spectroscopy: The non-resonant Raman spectrum of MoS_2 shows two peaks corresponding to the E^1_{2g} (388 cm^{-1}) and A_{1g} (407 cm^{-1}) modes [16–18]. The distance between these two peaks is a fingerprint of the number of layers in MoS_2, being 19 cm^{-1} for the single-layer limit. This way, it is possible to assign the number of layers for flakes of up to 10 layers (25 cm^{-1}). For more than 10 layers Raman spectroscopy is not an appropriate technique since the distance between peaks does not change (Figure 3.8-a and b). Additionally, there is a low intensity peak at 452 cm^{-1} corresponding to the 2^{nd} order mode 2LA, more intense for resonant excitation or for the presence of disorder.

The Raman process efficiency can be enhanced using an excitation energy resonant with the semiconducting gap or plasmon resonances. In MoS_2, the presence of the visible gap gives a real energy state instead of a virtual

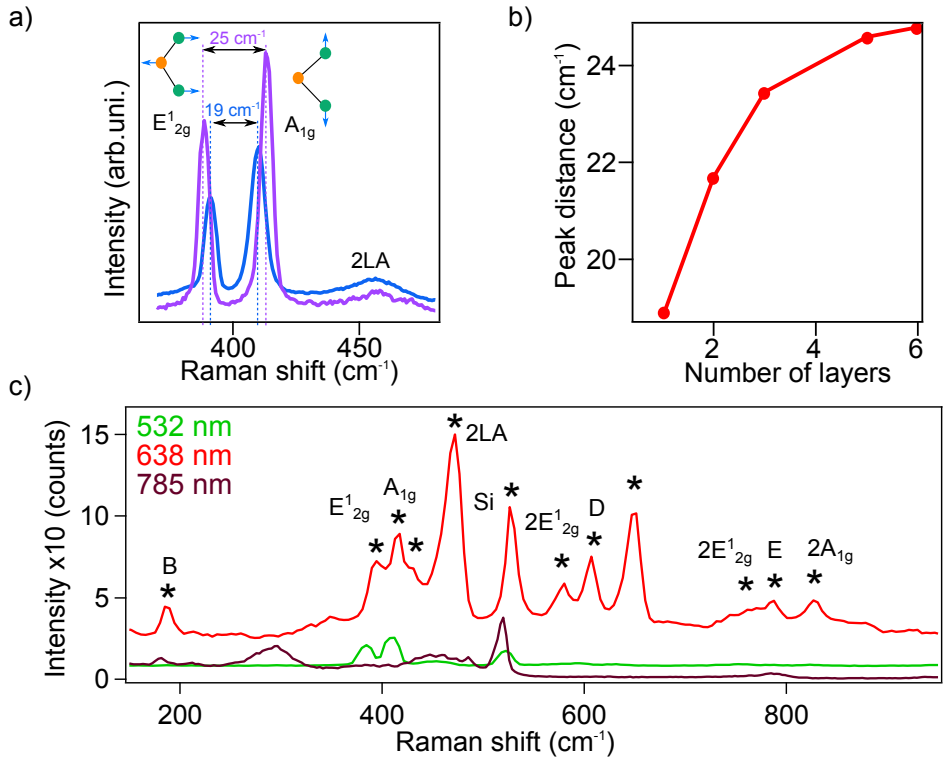

Figure 3.8: a) Raman spectra for 1L-MoS_2 and 6L-MoS_2, measured with 532 nm excitation. b) Raman shift difference between both modes as a function of the number of layers. c) Raman spectra for different excitation wavelengths: green (532 nm), red (638 nm) and deep red (785 nm). Data measured at the Freie Universität Berlin.

one what increases the efficiency of the process. One problem of resonant Raman spectroscopy is the co-existence of the photoluminescence, also enhanced by the resonant excitation, and the Raman signal. For 1L-MoS_2 the intense QE of photoluminescence screens the Raman signal whereas for few layers the lowering of intensity exposes the Raman signals.

The efficiency of the resonant excitation and the appearance of second order modes is compared with the signal obtained under non-resonant excitations. The direct gap of MoS_2 has an energy of 1.9 eV (640 nm), so the Raman spectrum of multilayer MoS_2 is measured for excitation energies bellow the gap energy (785 nm), in resonance (638 nm) and above the gap energy (532 nm) (Figure 3.8-c). The Raman spectrum when the excitation is bellow the gap energy (785 nm), only shows the modes corresponding to the Si substrate ($\approx 520\ cm^{-1}$). The spectrum obtained for the excitation

above the gap energy (532 nm), presents the two MoS_2 modes presented before and also the peak corresponding to the Si mode. However, the resonant excitation Raman spectrum shows other peaks assigned to 2^{nd} order processes (red spectrum in figure 3.8-c)).

WSe_2 Raman spectroscopy: The position and activation of Raman modes change from one material to other. In the case of WSe_2 the distance between the peaks corresponding to the E^1_{2g} ($256\ cm^{-1}$) and A_{1g} ($265\ cm^{-1}$) modes, does not change with the number of layers, but the intensity ratio of these two modes increases with the number of layers what can be used to determine the number of layers (Figure 3.9-c). Moreover, the B_1^{2g} mode marked with a red star, does not appear in the single layer limit, increases for few layers and vanishes again for bulk-like flakes (Figure 3.9-a). The absence of the B_1^{2g} mode together with the optical contrast is the most reliable method to identify mono-layers of WSe_2 [16, 17].

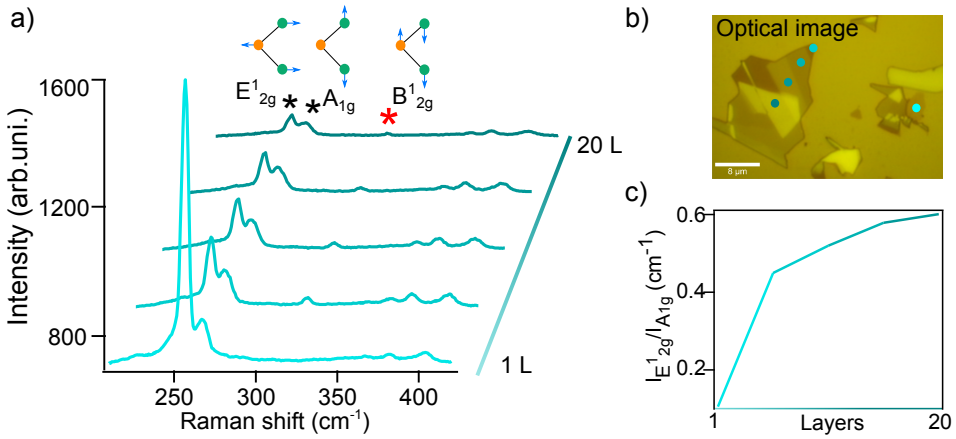

Figure 3.9: a) Raman spectra for different number of layers, measured with 532 nm excitation. b) Optical image of a WSe_2 flakes showing the different contrast of the different number of layers. c) E^1_{2g}/A_{1g} modes intensiy ratio for different layers.

The possibility of determining the number of layers for both MoS_2 and WSe_2 through Raman spectroscopy has been demonstrated, showing the high value of this non-destructive technique. In this thesis, Raman spectroscopy is used to identify the number of layers of each flake before the stamping and later device contacting.

$NbSe_2$ Raman spectroscopy: The crystalline structure in 2H-TMDs is similar only with variation on the lattice constants depending on the forming elements. Thus, the Raman active modes in $NbSe_2$ are also the E^1_{2g} and the A_{1g}, appearing at 178 and 234 cm^{-1} respectivelly [19]. To resolve

the active vibrational modes, the Raman spectrum of $NbSe_2$ is acquired after the excitation with different wavelengths (532, 638 and 785 nm, 2.33, 1.94 and 1.58 eV respectively) (Figure 3.10-a).

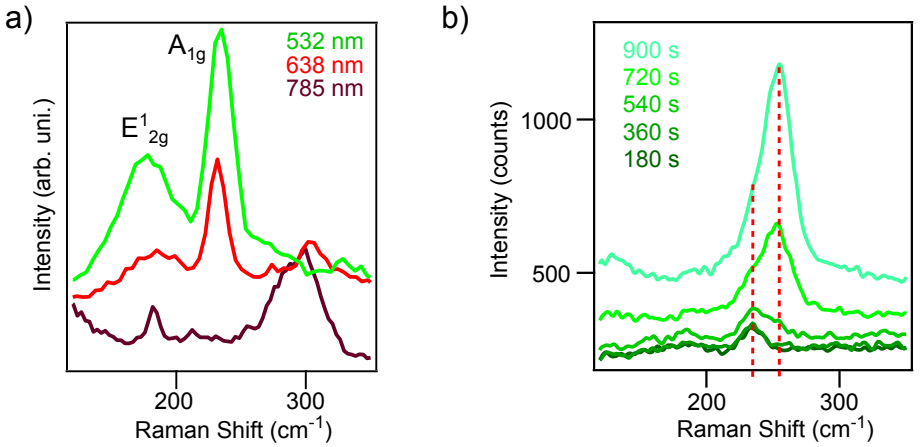

Figure 3.10: a) Raman spectra of $NbSe_2$ for different excitation wavelengths: green (532 nm), red (638 nm) and deep red (785 nm). b) Time evolution of the Raman spectrum of $NbSe_2$ under 532 nm excitation.

The excitation with 785 nm does not show any of the modes, probably because the excitation energy is too low to produce efficient Raman excitation. However, in the spectra obtained under 532 and 638 nm excitation both modes appear. Each spectrum was acquired with a different setup and thus the intensity of each mode are not comparable (Figure 3.10-a).

The MoS_2-$NbSe_2$ heterostructures studied in this thesis are prepared using a thick flake of $NbSe_2$. This way it is possible to avoid an increment of the device resistance produced by an oxide layer of $NbSe_2$. The optical characterization of the samples are typically done with low power excitation, 40 μW, avoiding any possible degradation of the samples. However, for this experiment, the time evolution of the Raman signal is measured for higher excitation power, 370 μW, in order to thermally induce the oxide formation or a degradation of the layers [79].

The evolution of $NbSe_2$ Raman spectrum is measured at high powers every three minutes, showing the appearance of a new peak near 255 cm^{-1} (Figure 3.10-b). In other studies of laser-induced degradation this new peak is assigned to the formation of a Nb-based oxide, Nb_2O_5 or NbO_2 [19,80,81].

3.2.2 Raman spectroscopy of heterostructure devices

Raman spectroscopy resolves lattice vibrational modes, giving information about the structural characteristics of the crystal. This way is possible to detect the thickness of materials such as MoS_2 and the identify the oxidation of $NbSe_2$.

Additionally, the lattice constant (a_0) for MoS_2 is 3.1475 Å and for $NbSe_2$ is 3.44 Å, what gives a lattice mismatch f of 8.5%, meaning that the lattice of the MoS_2 layer is expected to get deformed. This could modify the intensity or position of the Raman active modes [80]. Hence, the Raman signal of the heterostructure devices is measured after all the sample preparation steps.

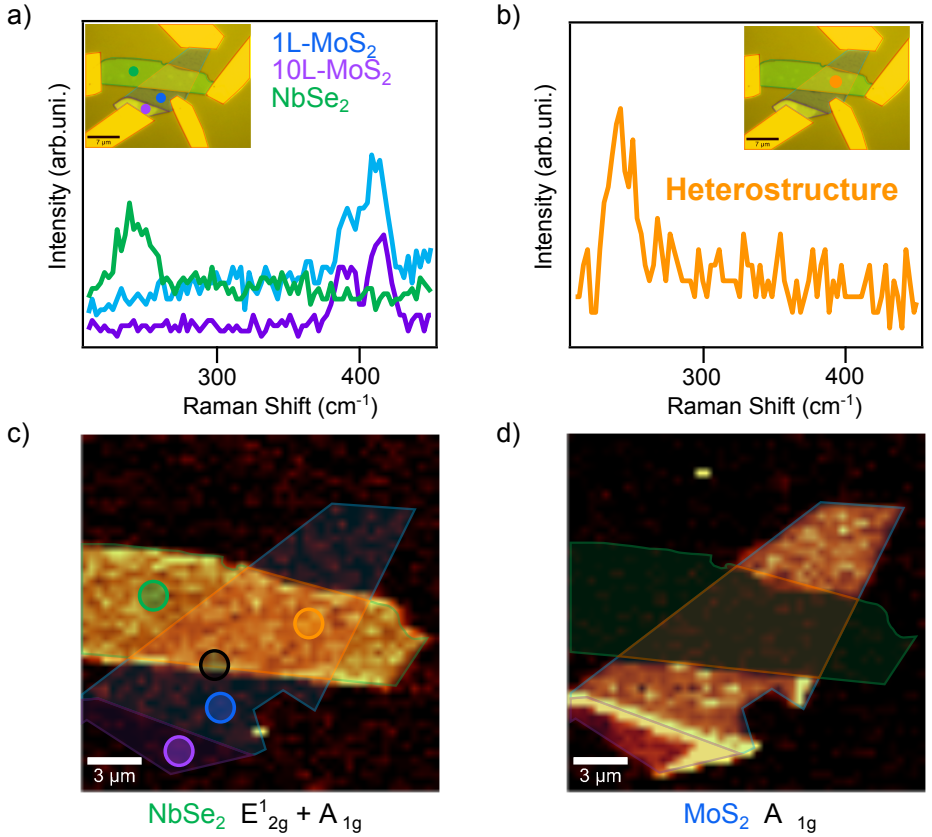

Figure 3.11: a) Raman spectra of 1L-MoS_2 (blue), 10L-MoS_2 (purple) and $NbSe_2$ (green) b) Raman spectra of the MoS_2-$NbSe_2$ heterostructure (orange). c) Raman intensity map integrating over $E^1_{2g}+A_{1g}$ modes of $NbSe_2$. d) Raman intensity map integrating over A_{1g} mode of MoS_2.

The Raman spectrum acquired on 1L-MoS_2, 10L-MoS_2 and on $NbSe_2$,

shows the characteristic Raman modes of both materials (Figure 3.11-a). For MoS_2, the spectra of both 1 and 10 layers contains two peak corresponding to the E^1_{2g} (388 cm^{-1}) and A_{1g} (407 cm^{-1}) active modes. Similarly, for $NbSe_2$ the spectrum exhibits a broad peak corresponding to both active modes (E^1_{2g} at 178 cm^{-1} and A_{1g} at 234 cm^{-1}). On the hybrid (1L-MoS_2/$NbSe_2$ area), the Raman modes of MoS_2 are totally suppressed due to the quenching produced by $NbSe_2$ (Figure 3.11-b).

The Raman intensity integrated over the $NbSe_2$ modes, shows an homogeneous spatial distribution of the intensity over the flake (Figure 3.11-c). On the contrary, the integration over the A_{1g} mode of MoS_2 shows the intensity vanished at the hybrid area (Figure 3.11-d). This corresponds to the quenching produced by $NbSe_2$ to MoS_2 observed for the MoS_2 photoluminescence (metal-semiconductor intensity quenching) [74–78].

3.3 Conclusions

In this chapter we succesfully characterized the photoluminescence of MoS_2 and WSe_2 and the Raman active modes of MoS_2, WSe_2 and $NbSe_2$ with a confocal microscope. We were able to determine the number of layers for MoS_2 and WSe_2 and that $NbSe_2$ degrades easily.

The photoluminescence intensity in MoS_2 increases as the number of layers decreases due to a change in the type of gap from indirect (bulk-MoS_2) to direct (1L-MoS_2). We observed the quenching of photoluminescence intensity when the single layer is on top of $NbSe_2$. For both MoS_2 and WSe_2 we observed higher resolution at low temperature. Finally, we obtained an inverted trend of the intensity, for WSe_2 (darkish material) is higher at RT and for MoS_2 (bright material) is higher at low temperature.

The Raman signal also changes with the number of layers, so we used it to determine the number of layers. In MoS_2 the distance between the peaks of the two main modes increases with the number of layers. While for WSe_2 it is the ratio of the intensity what increases with the number of layers. For this material a new vibrational mode appears with the number of layers. In the case of $NbSe_2$, it is posible to determine the oxidation of the material by measuring a new peak associated to the oxide.

Chapter 5

Spin-valley coupling in monolayer TMDs

In many two-dimensional semiconducting TMDs the band gap appears at the K point. The strong spin orbit coupling (SOC) and the broken symmetry in the single layer limit make the gaps in K and K′ point distinguishable. Therefore, the electrons are described not only by their charge and spin but also by the extra degree of freedom called "valley". This gave raise to a new field with applications in information encoding and processing, called "valleytronics". Most of the research lines efforts are devoted to obtain devices able to produce a current coming exclusively from one of the valleys.

This chapter is focused on the study of the valley pseudo-spin in 1L-WSe_2 on two different substrates. First the polarizability and Zeeman effect of WSe_2 on SiO_2 are characterized under an out-of plane magnetic field and different excitation polarizations. Moreover, we aim at characterizing and correlating the helicity of the valley pseudo-spin with the effective field created by the magnetic domains of a ferrimagnetic material used as substrate. Our goal is also to see if it is possible to address an increment of the polarizability or Zeeman splitting by applying an external magnetic field up to 5 T in the out-of plane direction. We found that the g factor and the polarizability observed for 1L-WSe_2 on the ferrimagnetic substrate is higher than the expected suggesting a possible exchange interaction between the two materials.

The valley properties were studied with a confocal microscope able to measure at variable temperatures, different external magnetic fields and two different excitation wavelengths (green and red). Moreover, the microscope was updated with a linear and circular polarization setup in order to measure the dependence of the optical signal for different polarization excitation and detection configurations. This setup was described in section 2.2.2.

5.1 Introduction to valley pseudospin in TMDs

Valleytronics is based on the possibility of accessing, manipulating and keeping valley pseudo-spin polarization information. Some of the most appealing properties from TMDs are their highly tunable optical properties, strictly related to their valley pseudo-spin properties. The main advantage of valleytronics comes from having one extra degree of freedom in addition to the charge and the spin: the valley.

In Mo and W based semiconducting TMDs the semiconducting gap appears at the K point, having two distinguishable valleys with opposite momentum, K-K′ (±K). The trigonal crystalline structure of the materials allows an inversion symmetry break for an odd number of layers, coupling the spin and valley pseudo-spin indexes. In the absence of magnetic field, the valleys are linked by time-reversal symmetry and thus are energetically degenerated. The magnetic moments of the different states, however, have opposite sign. The combination of strong spin orbit coupling and broken inversion symmetry in 1L-TMDs is the main reason to obtain nonequivalent gaps (valleys) at K and K′ [9, 10, 38].

The difference in angular momentum between the valley pseudo-spins enables to selectively access and populate one of the valleys by circularly polarized light. In this direction, it has been demonstrated the ability to electrically generate and control valley electrons in a two-dimensional semiconductor [11]. However, there are still many unanswered questions about the intrinsic valley properties before achieving a full electrical control over the population of valley electrons.

5.1.1 Origin of the valley pseudo-spin degree of freedom

The high d-orbital character coming from the metallic element (Mo or W) gives these materials a very strong spin-orbit coupling. This strong spin-orbit interaction energy produces an energy splitting of the order of hundreds of meV for the valence bands and tens of meV for the conduction bands. Interestingly, the split has opposite sign for W- and Mo-based TMDs [59].

In WX_2 materials, WSe_2 more specifically, the spin-orbit splitting of the conduction band is negative and thereby the spin up (down) appears in the highest (lowest) energy spin-splitted valence band (Figure 5.1-a). The spin of the lowest CB is opposite to the highest VB. In contrast, the conduction band of MoX_2 materials, in particular MoS_2, is not spin-inverted and the lowest energy of the conduction band has the same spin orientation as the highest split band in the valence band (Figure 5.1-b).

The spin splitting of the bands and the different momentum for each

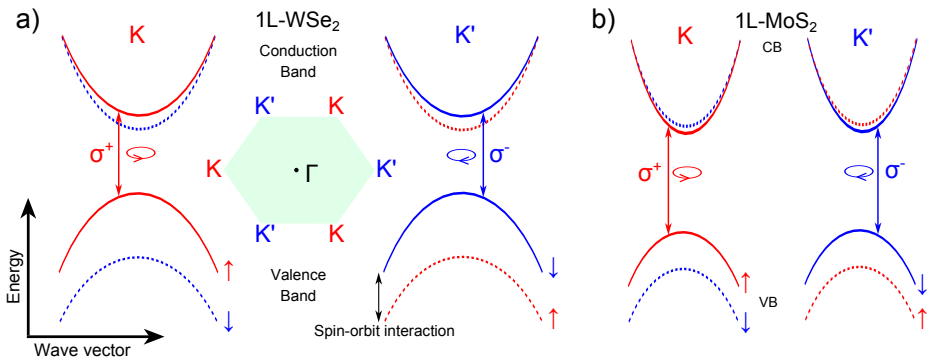

Figure 5.1: Schematic picture of the conduction and valence band splitting in K and K′ points of a) W based TMDs and b) Mo based TMDs.

valley results in a certain number of bright and dark transitions for both MoX_2 and WX_2 materials. The bright transition, radiative recombination of the exciton, only appears when both electron and hole have the same spin. In WSe_2 the bright exciton is generated between an electron and a hole from the upper spin-splitted level of the conduction and valence band (solid bands in K and K′). This corresponds to the transition marked in red (blue) in K (K′) valley in figure 5.1-a. The transition between the low spin-splitted CB (dashed band) and the higher VB (solid band) is a dark transition because spin is not preserved.

The fact that the transition between the closest levels is dark hinders the photoluminescence at low temperatures for WSe_2, when the excited electrons are relaxed to the lowest level of the conduction band, the dark level (See section 3.1.1). Contrary, the photoluminescence intensity of MoS_2 is higher at low temperature [62–64].

As it has been mentioned before, excitons from K and K′ valleys are formed by electron-hole pairs with different magnetic moment signs, creating a valley-dependent optical selection rule that allows a selective access to the valley degree of freedom by optical helicity. The illumination of WSe_2 with left (right) circularly polarized light, creates electron-hole pairs exclusively in the K (K′) valley. Photoluminescence is a process coherent with the excitation. Hence, the recombination of e-h pairs from the K (K′) valley produce left (right) circularly polarized photoluminescence (Figure 5.1-a) [116].

The recombination of excitons from the different valleys produces photoluminescence with opposite polarization but with the same energy. However, an out-of-plane magnetic field induces the breaking of time reversal symetry and shifts the bands differently depending in their pseudo-spin. Hence, the

photoluminescence produced in K and K′ has different polarization and different energy.

5.1.2 Magnetic field induced Zeeman splitting

In the absence of an external magnetic field, excitons and trions from both valleys (K or K′) have identical energy as expected from time reversal symmetry basis (Figure 5.2-b). However, the bands in which the excitons are created have a d-orbital character, for which the orbital magnetic moment points in the out-of-plane direction. Therefore, a magnetic field in this direction will couple to the magnetic moment of the single layer and break the valley degeneracy (Figure 5.2-a and c). An out-of-plane magnetic field leads to a shift in energy for each valley that depends linearly on B.

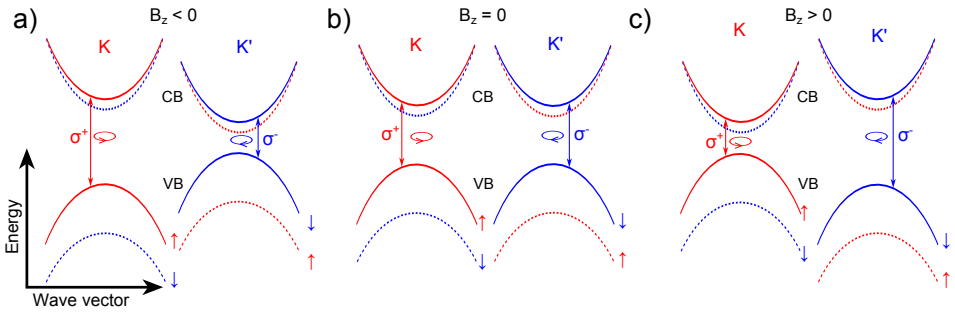

Figure 5.2: Schematic picture of the conduction and valence band splitting in K and K′ points of WX_2 under B_z: a) < 0 b) $= 0$ c) > 0. The Zeeman splitting produced by an out-of-plane magnetic field.

There are three possible contributions to the B-induced splitting: from the spin, pseudo-spin and orbital contribution of the metal [9,10]. The spin magnetic moment does not contribute to the energy shift in the photoluminescence because the selection rules only allow emission from transitions that conserve spin. A magnetic field produces the same shift to bands with the same spin ($\Delta_s = 2s_z\mu_B B$).

The atomic orbitals contribution ($\Delta\alpha = m\mu_B B$) affects the optical resonances. Since the conduction band is mainly composed of d-orbitals with m = 0 and the valence band by d-orbitals with m = 2 (-2) in K (K′), only the valence band is affected. This gives a shift of the optical resonance of -$2\tau\mu_B B$, where τ can be positive or negative for K or K′.

The valley magnetic moment (pseudo-spin) cause shifts with magnetic field as $\Delta_v = m\tau B$, with $m\tau = g_i\tau_z\mu_B$ (g_i is the valley g-factor for the conduction band (i = c) or the valence band (i = v)). The different value of the valley g-factor for the CB and VB ($g_c \neq g_v$), results in different

magnetic moments. Following this, the valley magnetic moment contributes by $\tau g_T \mu_B B$, with $g_T = g_c$ - g_v.

Since both the orbital and the pseudo-spin magnetic moment affect the optical resonance, the total shift has contributions from both (-$2\tau\mu_B B$ + $\tau\Delta\alpha\mu_B B$) with $\tau = 1$ (-1) for K (K′). Hence, a magnetic field induces a valley Zeeman splitting of:

$$\Delta \text{ E} = 2(2- g_T)\mu_B B \tag{5.1}$$

The differences on the optical resonances and the helicity of the transitions allows to distinguish between the emission from one or other valley (Figure 5.2-a,c). As a convention for this chapter, a negative (positive) out-of-plane magnetic field blueshifts (redshifts) the resonance in K (K′) valley while the K′ (k) transition redshifts (blueshifts) (Figure 5.2-a and c).

The Zeeman splitting in equation 5.1 is obtained from the different magnetic moment contributions of the initial and final states of the conduction and valence band to the optical transitions, giving a similar response for excitons and trions, since the extra electron adds a similar contribution to both initial and final states magnetic moments. However, whether the trion has the same response under an external magnetic field or not is still under investigation.

5.2 Polarization and splitting of valley in WSe_2 on SiO_2

The optical helicity of the emission is linked to the valley index of the electron-hole pairs. The photoluminescence signal of WSe_2 on a Si-SiO_2 substrate is collected in a Faraday geometry for different detection configurations. I_{co} ($I_{counter}$) is the photoluminescence signal detected with the same (opposite) circular polarization as the excitation (for experimental details see Section 2.2.2). In order to selectively excite the valley pseudo-spin, the green excitation is circularly polarized (left and right) and compared with a linearly polarized excitation (Figure 5.3).

In the absence of an external out-of-plane magnetic field the K and K′ valley transitions are indistinguishable in energy due to the time reversal symmetry protection. Therefore, independently of the excitation polarization both the intravalley and the intervalley transitions have the same energy (≈1.66 eV) (Figure 5.3).

In linear polarization, the parallel detection measures the intravalley recombination process (blue and red lines in figure 5.3-d) and the cross

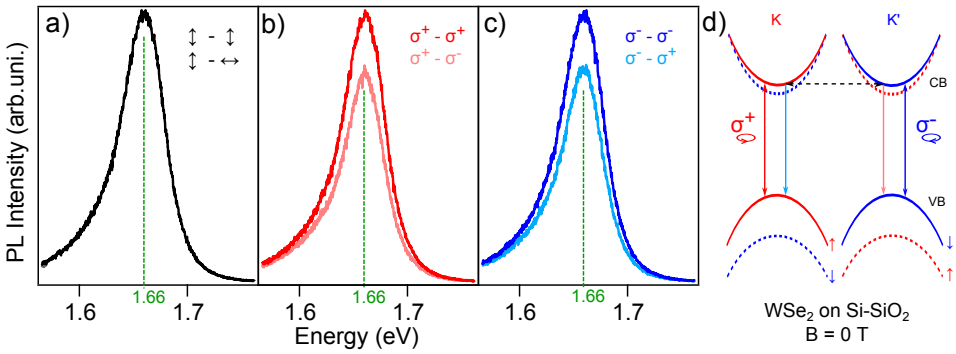

Figure 5.3: Photoluminescence spectra for: a) Linearly polarized light and parallel detection b) Left circularly polarized light, co- and counter-rotating detection. c) Right circularly polarized light, co- and counter-rotating detection. d) Band diagram of the valleys in K and K′ under no magnetic field.

detection the intervalley processes (light blue and light red lines in figure 5.3-d). Similarly, I_{co} detects the intravalley processes while with $I_{counter}$ we analyze the intervalley recombinations.

Linearly polarized excitation promotes electrons randomly in both K and K′ valleys so the valley polarization is not conserved. Therefore, both cross and parallel detection give the same intensity (Figure 5.3-a). On the contrary, the intensity of the intravalley transitions is higher than the intervalley transitions for circular polarization excitation and detection (Figure 5.3-b and c).

The electrons excited by left circularly polarized light (blue) are promoted from the valence band in K′ to the conduction band in K′ and mainly recombine in the same K′ valley. With a certain probability these electrons can also flip the pseudo-spin to the conduction band in K and emit in the opposite polarization (Figure 5.3-d). From the spectra in panels b and c, the degree of valley polarization ($P = (I_{co} - I_{counter})/(I_{co} + I_{counter})$) can be calculated. The polarization is 11% and is similar for both left and right polarization excitation (Figure 5.3-a, c).

Ideally, a material might have a 100% degree of valley polarization (P), giving no photoluminescence intensity for the counter-rotating configuration. However, the thermally or defect mediated intervalley scattering transitions decrease the polarizability in TMDs, increasing the counter-rotating signal.

The polar plots in figure 5.4 present the evolution of the photoluminescence intensity and energy of exciton and trion for σ^+ and σ^- excitation.

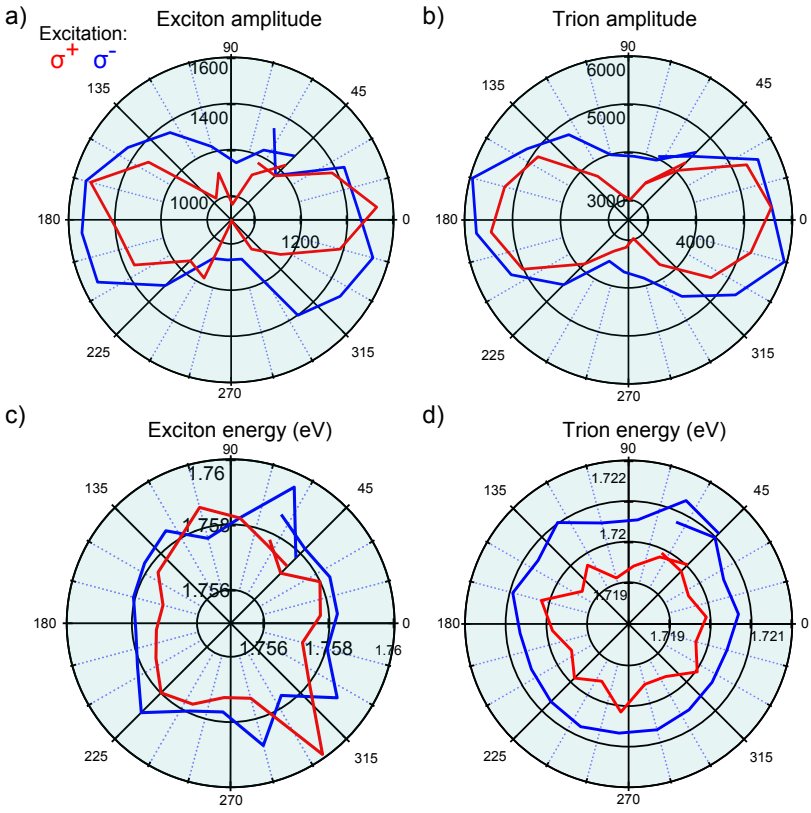

Figure 5.4: 1L-WSe_2 flake on SiO_2 substrate. a) Exciton amplitude. b) Trion amplitude. c) Exciton energy. d) Trion energy. Measurement conditions: 2 K, 0 T, left (red) and right (blue) circularly polarized light. Intensities normalized to the exposure time (arb. uni.) and the energies in eV.

Here, the photoluminescence spectrum is acquired at 2 K, while the analyzer is turned measuring I_{co}, $I_{counter}$ and the intermediate configurations. Low temperature photoluminescence measurements allows to identify not only the exciton (E) but also the trion (T) and the localization peaks of WSe_2. Both excitons and trions follow a similar trend in our measurements.

The main consequence of the valley polarization observed in the polar plots is the drop of intensity at 90 and 270 detection angles (Figure 5.4-a and b). In these detection angles I_{co} is measured and hence, the intervalley relaxation processes. Similar to the observation at RT in figure 5.3, in the absence of external magnetic field, the intravalley and intervalley relaxation processes have the same energy; no Zeeman splitting. Thus the polar plot the both exciton and trion energies is circular, similar energy for co- and counter rotating detections (Figure 5.4-c and d).

Magnetic field induced Zeeman splitting: In order to prove the effect of a magnetic field on the photoluminescence valley resonances, the samples were measured under out-of-plane magnetic fields between ± 5 T. An out-of-plane magnetic field should be responsible of a gradual shift in the photoluminescence resonance.

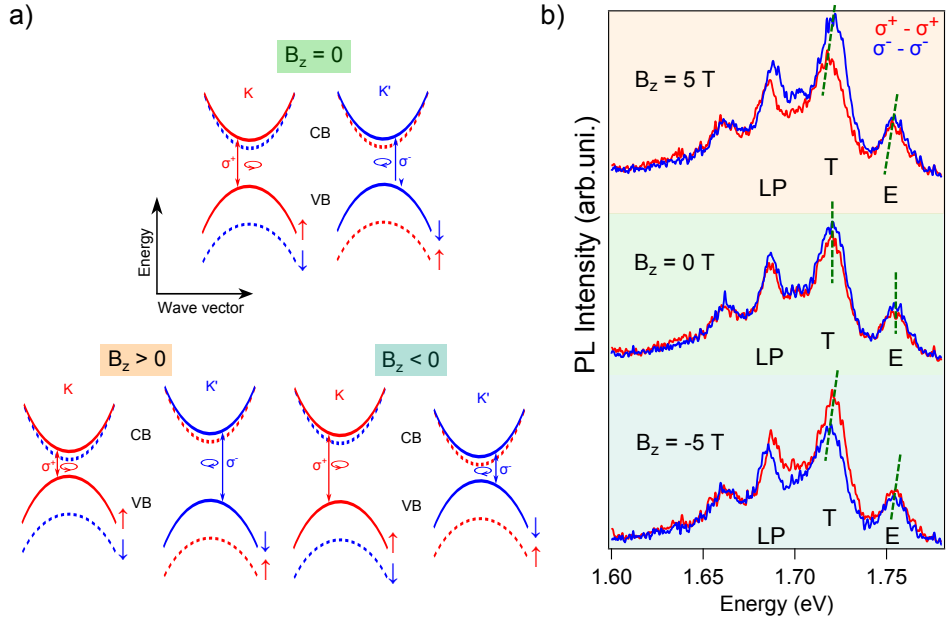

Figure 5.5: a) Band diagram of the valleys in K and K′ for different magnetic fields. b) Photoluminescence spectra at 2 K, under ±5 T and 0 T out-of-plane magnetic field for WSe_2 on SiO_2 substrate and green excitation wavelength.

In particular a positive magnetic field induces an energy increase of the K′ resonance while lowering the energy of the transition in the K valley (Figure 5.5). Additionally, a σ^+ photon has an spin angular momentum pointing in the positive magnetic field direction, exciting electrons in the K valley (Figure 5.5-a). As a consequence, the resonances observed under σ^+ excitation are less energetic for positive magnetic fields than for negative (Figure 5.5-b upper panel). Since the valleys are linked by time reversal symmetry, under a positive magnetic field, the excitation with σ^- polarization excite the more energetic transitions (Figure 5.5-b lower panel). The energy shift are clearer when compared with the spectra acquired in the absence of a B_z field (middle panel).

In order to study the evolution of the valley polarization (P) with magnetic field, the photoluminescence signal is measured in co- and counter

rotating detection for both σ^+ and σ^- excitations. The value of P is almost independent on the excitation polarization, but depends on the magnetic field. The polarization under an external magnetic field (10%) is higher than the polarization under no external magnetic field at 2 K (3%).

5.3 Valley splitting of WSe_2 on a ferrimagnetic substrate

Photoluminescence experiments with circularly polarized light are a direct measurement of the valley polarizability and the Zeeman effect as a consequence of the optical helicity of the valley emission. Here we investigate the effect of a ferrimagnetic material on the optical valley properties of a 1L-WSe_2. The aim is to explore the existence of an exchange field interaction from the stray field of the magnetic domains of the substrate.

The samples were prepared by mechanical exfoliation of WSe_2 crystals using PDMS and deposited with an stamping setup on YIG (Yttrium Iron Garnet, $Y_3Fe_2(FeO_4)_3$, provided by INNOVENT e.V) substrates (for sample preparation see chapter 2.1). YIG is a ferrimagnetic material in wich the yttrium (III) ions are coordinated to eight oxygen atoms in an irregular cube. The iron (III) ions sit on two octahedral and three tetrahedral positions. In our experiments, we used 2 μm of YIG grown on GGG (Gadolinium Gallium Garnet, $Gd_3Ga_5O_{12}$) (Section 5.4). Since YIG is a ferrimagnetic material, it has a magnetic domain arrangement with a periodicity of 2 nm with a magnetic moment pointing up or down in the out-of-plane direction (Figure 5.6-a).

The stray field of the YIG substrates used for these experiments is considered to be around 1 T [117]. This magnetic field is expected to produce a small Zeeman splitting, close to the energy detection limit of the spectrometer. However, exchange field interaction might increase the effective magnetic field enabling the manipulation of the valley pseudo-spin at room temperature.

The photoluminescence spectra of WSe_2 on SiO_2 and YIG have different intensities (Figure 5.6-b). The multiple internal reflexions on the SiO_2 film increases by orders of magnitude the external quantum efficiency (EQE) of the photoluminescence. Moreover, the interaction between flake and substrate also affects the photoluminescence intensity and energy. Previous experiments have found a photoluminescence quantum yield (QY) around 10 times higher for TMDs flakes on h-BN [38].

The relative intensity between the exciton and the trion $((I_E\text{-}I_T)/(I_E+I_T))$ is higher for WSe_2 on YIG (0.5) than on SiO_2 (0.3). The interaction of the single-layer with the substrate can change the doping of the material in-

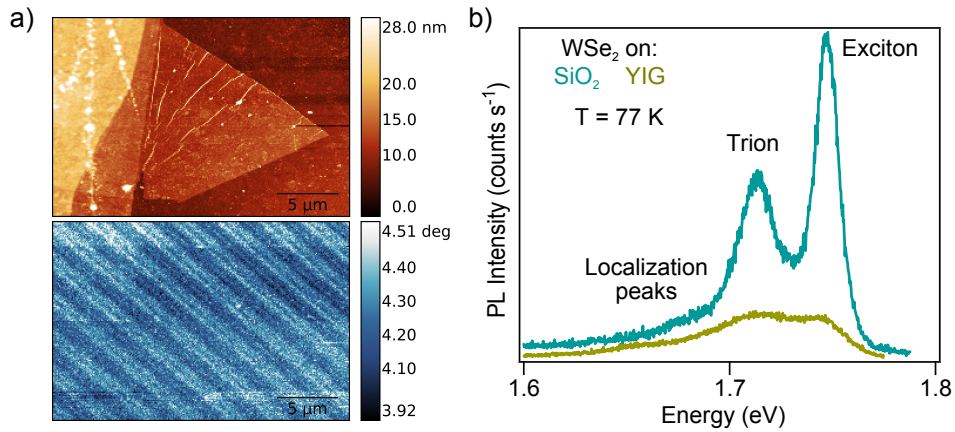

Figure 5.6: a) AFM image of the 1L-WSe_2 flake and MFM image of the magnetic domains with a periodicity of 2 μm. b) Photoluminescence spectra of 1L-WSe_2 on SiO_2 (blue) and YIG (pistachio), measured at 77 K, using a green excitation laser.

creasing the number of unpair charges. This increases the probability of an exciton forming a trion, reducing the exciton intensity (Figure 5.7). The samples are not contacted so is not possible to identify the nature of the trion (positively or negatively charged exciton). However, since WSe_2 typically appear as a p-doped semiconductor, the trion is expected to be a positive trion due to the extra holes in the material.

The optical response of 1L-WSe_2 on YIG is analyzed with circularly polarized light and under magnetic fields and also with two different excitation wavelengths (red, He-Ne laser, 633 nm-1.96 eV and green, 532 nm-2.33 eV). The common approach to these experiments is to use an excitation energy close to resonance in order to avoid polarizability losses due to inter-valley relaxation processes and also minimize non-radiative decays. However, due to experimental issues (section 5.4), the polarization and magnetic field dependence photoluminescence measurements were done with a non-resonant and continuous-wave green laser (2.33 eV - 532 nm). The excitation is focused on the sample by an objective with a spot size of few microns, with a power of $\approx$100 μW (Section 2.2 for experimental setup details).

In order to excite and analyze the signal in linear and circular polarization basis the excitation and the emission pass through a set of linear polarizer, $\lambda/2$ and $\lambda/4$ wave retarders, before it gets into a spectrometer. The spectrometer has three different grids and is equipped with a CCD detector. The measurements were carried out in a cryostat (commercially available Attocube confocal microscope with modifications in the optical

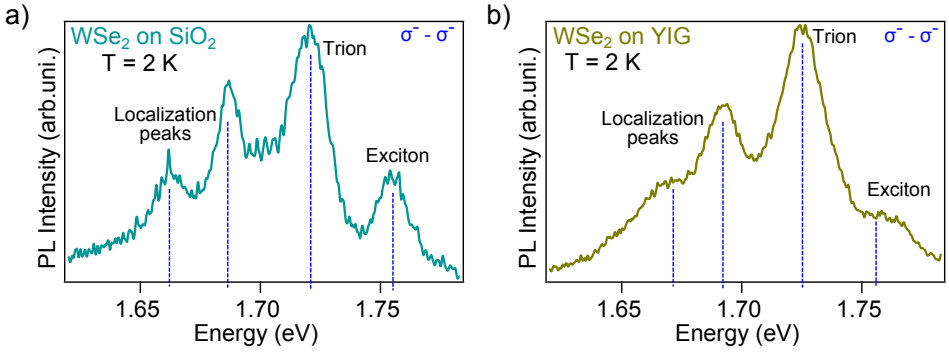

Figure 5.7: Photoluminescence spectra of 1L-WSe_2 on: a) Si/SiO_2 (blue) and b) YIG (pistachio), measured at 2 K, using a green excitation laser.

setup) in order to perform variable temperature analysis under an out-of-plane magnetic field ranging from - 5 T to + 5 T. The sample is mounted on a XY piezo stage to analyze the spatial distribution of the photoluminescence signal (See Section 2.2.2).

5.3.1 Valley splitting of WSe_2 on a ferrimagnetic substrate

The main objective here is to study the effect of the ferrimagnetic substrate (YIG) on a WSe_2 single-layer. The different interaction between WSe_2 and the substrates produces a different doping regimens, changing the relative intensity between the exciton and trion peaks for each substrate. YIG is an insulator material in which we observed a high EQE of the trion, corresponding with a high-doping of WSe_2. In this high-doping regime with a weak exciton peak more information can be extracted from the trion resonance [118]. The results obtained for the trion are similar to the observations for the exciton so in this section we focus on the trion emission.

Circularly polarized excitation and detection: In the absence of an external magnetic field (experiments of WSe_2 on SiO_2), the optical transitions are expected to maintain the same energy independently of the polarization. Therefore, it is only possible to distinguish between K and K′ valley transition by means of circularly polarized light. However, the effect of the ferrimagnetic substrate should, in principle, induce a Zeeman splitting and an increment of the polarizability.

Contrary to expected, the trion energy is around 1.7 eV and is similar for all the detection configurations so apparently there is no measurable effect from the stray field (circular shape of the polar plot in figure 5.8-a). The absence of Zeeman splitting indicates that the effect is too small to be detected or that a different effect hinders it. The different energy of the

trion obtained for left (red) and right (blue) excitation, probably appears due to instabilities of the setup.

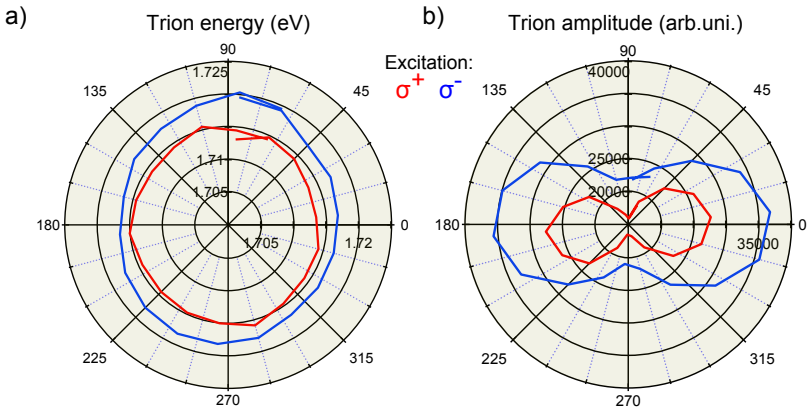

Figure 5.8: Polar plot of the photoluminescence a) energy (eV) b) amplitude (arb.uni.), of the trion in 1L-WSe_2 flake on YIG. Measurement conditions: 2 K, 0 T, excitation with left (red) and right (blue) circularly polarized light. Intensities normalized to the exposure time (arb.uni.) and the energies in eV.

The photoluminescence intensity of the trion measured in co-rotating, I_{co}, is higher than in counter-rotating, $I_{counter}$, with the polarizability around 30% (Figure 5.8-b). Interestingly, the intensity obtained under left (red) circular polarized excitation is lower than the obtained under right (blue) circular polarization. This effect also appears when the sample is under an external magnetic field. However, this difference can also be caused by fluctuations in the experiment, supporting the absence of Zeeman splitting.

Magnetic field induced Zeeman splitting: An external out-of-plane magnetic field couples to the magnetic moments of the d-orbital in WSe_2 producing a Zeeman splitting. Figure 5.9-a and b show the evolution of WSe_2 photoluminescence spectrum as an out-of plane magnetic field is changed from -5 T to 5 T.

The excitation with σ^+ (panel a) polarization generates excitons in the K valley while σ^- (panel b) excites the K′ excitons. For a negative B field the K valley has a higher energy than K′. As a consequence, the spectra in panel a redshift and in panel b blueshift when increasing the B field. The energy shift is indicated in the intensity plots of figure 5.9-a and b, with vertical tilted lines. For clarity, in panel c we plot the spectra corresponding to the blue and black asterisks.

To evaluate the g-factor, the Zeeman splitting ($\Delta E = E_{co}$ - $E_{counter}$) is ploted for different magnetic fields. The spectra obtained for the co- and the

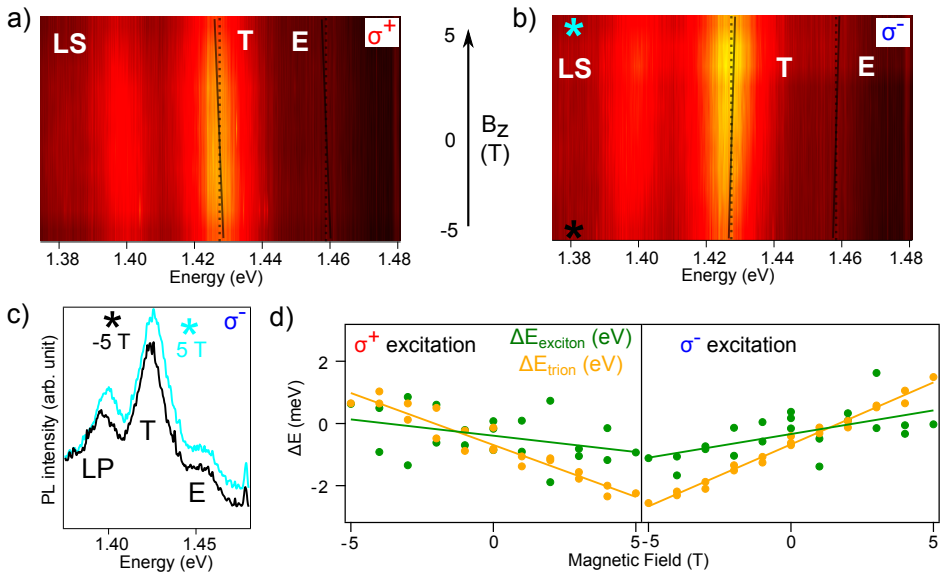

Figure 5.9: a, b) Photoluminescence spectra, exciton (E), trion (T) and localized states (LP), of ML-WSe_2 for left and right green CPL, in co-rotating measuring configuration as a function of an external perpendicular magnetic field. c) Corresponding photoluminescence spectra acquired under -5 t (black) and 5 T (light blue) for σ^- excitation d) Energy of the Zeeman splitting (ΔE) of exciton and trion (calculated as the difference of E_{co} and $E_{counter}$) as a function of an external perpendicular magnetic field.

counter-rotating configuration are fitted to 4 Lorentzian functions (exciton, trion and two localized states) to obtain the energy of each transition (E_{co} and $E_{counter}$ of the exciton and trion).

The valley Zeeman splitting (ΔE) was described in equation 5.1 as 2(2-g_T) μ_B B, where g_T is the effective g-factor of the resonance, μ_B is the Bohr magneton and B the magnetic field. The value of the g-factor, estimated from the linear fit in figure 5.9-c, is around 1 for both exciton and trion (for WSe_2 on SiO_2 we also observed $g_T = 1$). The the g-factors reported in literature for the different photoluminescence resonances in WSe_2 are larger than our observation, between g = 4 and g = 12 [9, 10, 62, 118–121].

Helicity under an external magnetic field: As it has been mentioned, the intervalley interactions determine the polarization degree (P = (I_{co} - $I_{counter}$)/(I_{co} + $I_{counter}$)). This can be obatained by measuring evolution of the photoluminescence spectrum with the detection angles for a given, σ^+ or σ^-, excitation (Figure 5.10-a). The evolution of the exciton is similar to the trion but with much lower intensity due to the high-doping regime observed for WSe_2 on YIG, hence we analyzed only the trion.

The polar plot of the trion intensity under σ^+ excitation for different detection angles is spheric in shape with a drop of intensity along the minor semi-axis (the a- polar plot). The intensity is higher at 0° and 180° corresponding to I_{co}, intravalley relaxation. The lower intensity at 90° and 270° correspond to intervalley relaxation processes, $I_{counter}$. The external magnetic field also modifies the intensity of the optical resonances through the break of intervalley interactions increasing the polarizability.

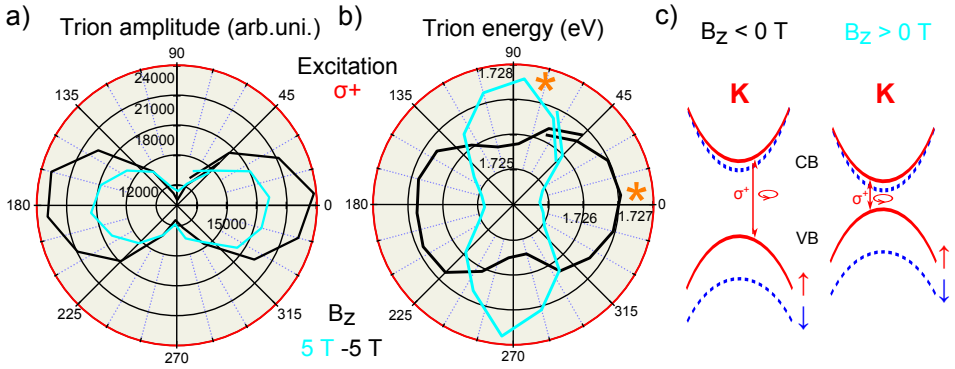

Figure 5.10: a) Trion amplitude b) trion energy of 1L-WSe_2 on YIG excited with left circularly polarized light (σ^+, K valley transitions) under -5 (black) and 5 T (light blue) out-of-plane magnetic field. c) Band diagram of the K valley under negative (black) and positive (light blue) magnetic field.

In section 5.2, we found that the polarizability of the exciton and trion for the WSe_2 on SiO_2 under a B field of 5 T is similar for both left and right circularly polarized light. However, the polarizability of the exciton and trion of WSe_2 on YIG is different for σ^+ and σ^- (table 5.1).

The intravalley transitions under σ^+ polarization excitation occur in the K valley. Under a positive magnetic field E_g decreases in K valley (Figure 5.10-c). Therefore, the electrons in the CB of the K valley need a flip on the pseudo-spin momentum and a gain of energy to produce intervalley interactions. This lowers the intervalley emission probability, higher polarizability for σ^+ excitation under positive magnetic fields. The effect is similar with σ^- excitation under negative magnetic fields.

As a consequence of the Zeeman splitting, the energies of the intravalley and intervalley trion are different under an out-of-plane magnetic field (Figure 5.10-b). The transition in the K point increases under negative magnetic field and lowers under positive B field (band diagram in panel c).

The 90° mismatch between the black and light blue lines observed in the trion energy polar plot (orange asterisks in figure 5.10-b) is caused by

	$P_{Exciton}$ ($B_z = 5$ T)		P_{Trion} ($B_z = 5$ T)	
	WSe_2 on SiO_2	WSe_2 on YIG	WSe_2 on SiO_2	WSe_2 on YIG
σ^+	14	24	19	22
σ^-	15	5	30	13

Table 5.1: Polarizability of 1L-WSe_2 exciton and trion on SiO_2 or YIG measured for σ^+ and σ^- polarizations under an out-of-plane magnetic fields of 5 T.

the different procedence of the trion. Under σ_+ excitation the co-rotating detection (0-180° axis) measures the K transitions (intravalley) while the counter-rotating detection (90-270° axis) measures the K′ transitions (intervalley). Thus, under σ^+ excitation the co-rotating detection (0-180° axis) is more energetic for negative magnetic field.

5.3.2 Spatial distribution of photoluminescence polarization

The magnetic field and polarization dependence of the exciton and the trion revealed the effective Zeeman splitting of WSe_2 on YIG under an applied magnetic field. In the inset of figure 5.11-b, the MFM image with the magnetic domains is overlapped with the AFM image of the flake. The positive and negative orientation of the magnetic domains should give a photoluminescence intensity modulation with a periodicity of 2 μm.

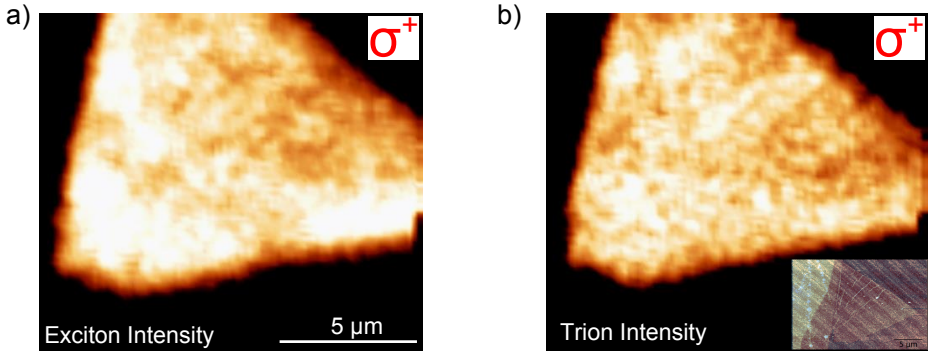

Figure 5.11: Photoluminescence intensity map integrating over the a) exciton peak b) trion peak. The map is acquired at 77 K with green left polarization (σ^+) excitation and no external magnetic field applied.

We measured the spatial distibution of the photoluminescence, to correlate the polarization with the stray field from the magnetic domains (Figure 5.11). Contrary to expected the photoluminescence intensity maps in figure

5.11 integrating over the exciton (panel a) and the trion (panel b) peaks do not show any periodicity, for what we found several explanations.

First; the green excitation is far from being resonant with the photoluminescence processes, losing the polarizability of WSe_2. To increase the polarizability, we also measured with a close-to-resonance red laser. However, due to experimental problems, it was impossible to measure the photoluminescence spectra of WSe_2 at low temperatures. The WSe_2 photoluminescence quenching will be explained in the next section (Section 5.4). We also measure with red excitation at room temperature to avoid the experimental problems, but the photoluminescence peaks are too broad to identify the different exciton and trion peaks and study the position and intensity of each resonance.

Second; the photoluminescence intensity maps of the exciton or trion do show areas with different intensities but not with the periodicity or shape of the magnetic domains. The ferrimagnetic substrate that we used, YIG, has a high roughness around 1-2 nm (for SiO_2 substrates is around 0.3 nm) measured by scanning tunneling microscopy and comparable with values found in literature [122]. The roughness of the substrate can induce strain on the 1L-WSe_2 flakes stamped on it. It has been reported that the strain can induce a pseudo-magnetic field, in some situations even greater than 300 T [39–44]. As a consequence, we think that the effect of the strain hinders any effect produced by the stray field from the magnetic domains.

5.4 Photoluminescence of impurities on garnets

The ferrimagnetic substrate used in this chapter is made of 2 μm of YIG on a GGG (gadolinium gallium garnet) substrate (Figure 5.12). Rare Earth Garnets (REG) are materials with a formula $A_3B_2C_3O_{12}$, in which A is a RE element (Gd^{3+}, Y^{3+}, Sc^{3+}) and B-C are transition metals from group III (Ga^{3+}, Al^{3+}, Fe^{3+}). The crystalline structure of both sides of the substrate (YIG on one side and GGG on the other one) are very similar as can be observed in the TEM image in figure 5.12-a. However, the properties of each material are very different. The YIG crystalline structure is formed by Y^{3+} and Fe^{3+} ions where the GGG has Gd^{3+} and Ga^{3+} ions.

These materials, some of them synthetic, can be efficiently doped with different ions modifying their magnet or optical properties. From the optical point of view, garnets typically show a high photoluminescence quantum efficiency. In fact, yttrium aluminum garnet (YAG) doped with Nd^{3+} ions are widely used as a lasing medium in laser industry. In GGG it is possible to introduce different dopants such as cerium, lutetium, manganese or chromium in order to modify its color and is a very optically active mate-

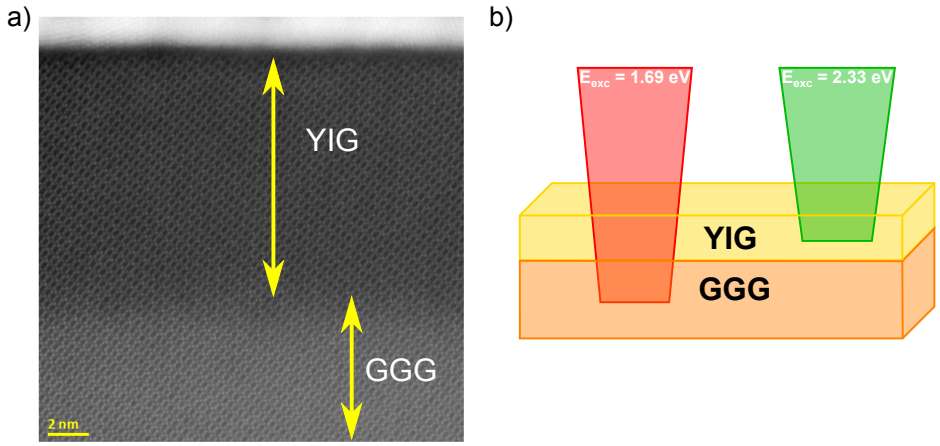

Figure 5.12: a) TEM image of the cross section direction of the YIG-GGG substrate. b) Squematic representation of the penetration of the different excitation wavelengths on the substrate. Acknowledgement to Saül Vélez et al. for the TEM image.

rial. YIG is an insulating ferrimagnetic material with an electronic gap in the order of 2-3 eV, more transparent to the red light (1.96 eV) than to the green light (2.33 eV) (Figure 5.12-b).

Most of the valley polarization measurements are done at low temperature to increase the energy resolution. In figure 5.13 the photoluminescence spectrum of 1L-WSe_2 on YIG is presented for red and green excitation as the sample is cooled down.

The photoluminescence spectra of WSe_2 under green excitation is similar to the ones measured on SiO_2 substrates (Figure 5.13). The only difference here is that the relative intensity of the exciton and the trion peaks is decreased due to different interaction with the substrate (Section 5.3). At low temperature it is possible to resolve the trion while at RT the spectra has only one peak redshifted from the exciton optical transition.

The photoluminescence spectra measured under red light excitation is similar at high temperature, appearing as a high and broad peak. In contrast, when lowering the temperature, additional sharp peaks appear at higher energies and broad peak at similar energy as WSe_2 resonances (Figure 5.13).

In literature these two peaks are assigned to Cr^{3+} dopants in GGG [123, 124]. To excite the optical resonances of Cr^{3+}, the excitation beam needs to pass through the 1L-WSe_2 and 2 μm of YIG (Figure 5.12-b). A single-layer of WSe_2 is equally transparent along the visible spectral range. However, YIG (E_g from 2-3 eV, thickness dependence) is less transparent

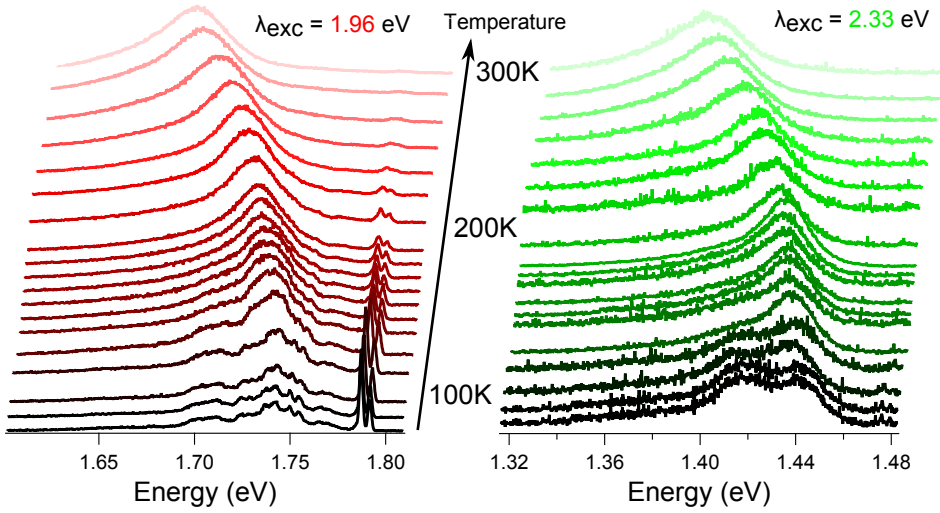

Figure 5.13: Temperature dependence PL of ML-WSe_2, measured under red and green laser excitation.

to green. As a consequence, the emission from Cr^{3+} dopants is negligible under green excitation.

The high intensity of the Cr^{3+} emission and the similar energy to WSe_2 resonances at low temperature, prevented us to measure the photoluminescence of WSe_2 under red excitation at low temperatures. An option to avoid this emission might be to use YIG substrates without GGG bellow or with thicker YIG on top. However, both options will modify the periodicity of the magnetic domains, complicating other experimental aspects. Since confocal microscopy is a diffraction limited technique, it would be not possible to see a periodicity of the magnetic domains lower than 500 nm.

5.5 Conclusions

In this chapter we characterized the valley polarizability of WSe_2 after the excitation with different polarizations and under different out-of-plane magnetic fields. Also, we intended to correlate the magnetic domains pointing in the out-of-plane direction of a ferrimagnetic substrate with the valley polarizability and Zeeman splitting.

For WSe_2 on SiO_2 under green excitation we obtained an 11% valley polarization under no magnetic field and for both left and right circularly polarized light. Under linear excitation the helicity information is lost due to the excitation of electrons in both valleys. Since WSe_2 is a darkish material the intensity at 2 K is lower but it is possible to resolve the exciton, trion

and the localization peaks. Under a magnetic field of 5 T we see a Zeeman splitting of 3.7 meV and a polarizability of 10%. We obtained a similar trend for the exciton and trion.

The photoluminescence is highly affected by the level of doping. For WSe_2 on YIG we observed a high doping effect and thus higher intensity for the trion. Since both exciton and trion follow a similar behavior we focused on the trion emission. In the absence of a magnetic field we saw a polarizability of around 30% (5% higher for left circularly polarized excitation). Under an external out-of-plane magnetic field we measured the Zeeman as a function of the applied magnetic field. This way we calculated the g-factor of WSe_2 on YIG with values between 1 and 2.

Finally, we mapped the photoluminescence spectrum expecting a periodicity of the signal following the magnetic domains of the YIG. At low temperature and under red excitation we observed very intense emission from Cr^{3+} impurities on the GGG substrate. Thus, we measured photoluminescence under green circularly polarized excitaiton. The roughness of the substrate produces a valley polarization that hinders the effect of the stray field of the magnetic domains. The excitation with green wavelength lowers the polarizability and as a consequence the probability of observing the effect.

It is possible to reduce the roughness of YIG by different treatments what in principle might help to reduce the strain to WSe_2. Additionally, WSe_2 flake can be stamped in a YIG crystal, eliminating the emission of Cr^{3+} impurities. The periodicity of the magnetic domains changes with the thickness of the material so it would be necessary to re-characterize of the magnetic signal.

Finally, the polarizers and wave retarders used in this chapter are all manually turned. In principle, this can produce fluctuations of the intensity as a consequence of small changes on the alignment. One solution is to use motorized components instead, increasing the reproducibility of the measurements.

Conclusions and Outlooks

We studied the optoelectronic response of MoS_2 in different devices: 1L-MoS_2, 1L/3L-MoS_2 isotype heterostructures and MoS_2-$NbSe_2$ heterostructures. In all of them the charge transfer from one material to the other produces a potential barrier at the junction.

For all the device we observed long photocurrent lifetime associated to trap charges in MoS_2 based devices. The mechanism of photocurrent generation varies with the position of the illumination. Under no V_{sd}, the built-in potential at the contacts produces photocurrent when exciting this area (photovoltaic effect). When the illumination is centered in the device, we need to apply an external V_{sd} to separate the electron-hole pair, photoconductivity. We prepared isotype heterostructures of MoS_2. The change of the energy gap with the number of layers generates a potential barrier at the junction between layers. The potential barrier between the layers blocks the current flow in one direction, rectifying response, increasing the on/off ratio of the dark current for forward and reverse voltage. Additionally, we managed to control electrically the photoluminescence intensity in MoS_2 devices.

The absence of an strong Fermi level pinning enables the generation of a very energetic Schottky barrier, observed in the photocurrent maps without applying an external V_{sd}. The transfer of electrons from MoS_2 to $NbSe_2$, p-doped the MoS_2 layer at the heterostructure obtaining p-n and n-p-n junctions. The DFT calculations further proved the band alignment proposed for the heterostructure. Moreover, the local illumination of the heterostructure showed a very high on/off response to light, related to the high Schottky barrier between.

In the future it might be interesting to measure the potential distribution on the heterostructure by Kelvin probe force microscopy (KPFM). The potential distribution will give an experimental evidence and quantitative characterization of the doping degree in MoS_2 over the device.

All the materials used in this thesis (MoS_2, WSe_2 and $NbSe_2$) are characterized by Raman spectroscopy and photoluminescence with a confocal microscope. The photoluminescence intensity in MoS_2 increases when de-

creasing the number of layers due to a change in the type of gap from indirect (bulk-MoS_2) to direct (1L-MoS_2). Also, the photoluminescence intensity quenches when the single-layer is on top of $NbSe_2$. For both MoS_2 and WSe_2 we observed higher resolution at low temperature, observing the exciton, trion and localized states. We obtained an inverted trend for the photoluminescence intensity, for WSe_2 (darkish material) is higher at RT and for MoS_2 (bright material) is higher at low temperature.

The Raman signal also changes with the number of layers, so we used it to determine the number of layers. In MoS_2 the distance between the peaks of the two main mode increases with the number of layers. While for WSe_2 is the ratio of the intensity what increases with the number of layers. For this material a new vibrational mode appears with the number of layers. In the case of $NbSe_2$, it is possible to determine the oxidation of the material by measuring a new peak associated to the oxide.

Additionally, we characterized the valley polarizability of WSe_2 after the excitation with different polarizations and under different out-of-plane magnetic fields. Also, we intended to correlate the magnetic domains pointing in the out-of-plane direction of a ferrimagnetic substrate with the valley polarizability and Zeeman splitting.

For WSe_2 on SiO_2 under green excitation we obtained an 11% valley polarization exciting with circularly polarized light and no polarizability after exciting with linearly polarized light under no magnetic field. Under a magnetic field of 5 T we see a Zeeman splitting of 3.7 meV and a polarizability of 10%, obtaining a similar trend for both exciton and trion.

WSe_2 on YIG is in a high-doping regime and thus the photoluminescence intensity of the trion is higher than the exciton. In the absence of a magnetic field we see a polarizability of 25% for right and 35% for left circularly polarized excitation. Under an external out-of-plane magnetic field we measured the Zeeman splitting as a function of the applied magnetic field. This way we calculated the g-factor of WSe_2 on YIG with values between 1 and 2.

Finally, we mapped the photoluminescence spectrum expecting a periodicity of the signal following the magnetic domains of the YIG. At low temperature and under red excitation we observed very intense emission from Cr^{3+} impurities on the GGG substrate. Thus, we measured photoluminescence under green circularly polarized excitation. The roughness of the substrate produces a valley polarization that hinders the effect of the stray field of the magnetic domains. The excitation with green wavelength lowers the polarizability and as a consequence the probability of observing the effect.

It is possible to reduce the roughness of YIG by different treatments what in principle might hep to reduce the strain to WSe_2. Additionally,

WSe_2 flake can be stamped in a YIG crystal, eliminating the emission of Cr^{3+} impurities. The periodicity of the magnetic domains changes with the thickness of the material so it would be necessary to re-characterize of the magnetic signal.

The polarizers and wave retarders used in this chapter are all manually turned. In principle, this can produce fluctuations of the intensity as a consequence of small changes on the alignment. One solution is to use motorized components instead, increasing the reproducibility of the measurements.

Bibliography

[1] A. Manjavacas, J. G. Liu, V. Kulkarni, and P. Nordlander, "Plasmon-induced hot carriers in metallic nanoparticles," *ACS Nano*, vol. 8, no. 8, pp. 7630–7638, 2014.

[2] . P. Alonso-González,1 A. Y. Nikitin,1,2 F. Golmar,1,3 A. Centeno,4 A. Pesquera,4 S. Vélez,1 J. Chen,1 G. Navickaite,5 F. Koppens,5 A. Zurutuza,4 F. Casanova,1,2 L. E. Hueso,1,2 R. Hillenbrand2, "Controlling graphene plasmons with resonant metal antennas and spatial conductivity patterns," *Science*, vol. 344, no. 6190, pp. 1369–1373, 2014.

[3] S. Dai, Q. Ma, M. K. Liu, T. Andersen, Z. Fei, M. D. Goldflam, M. Wagner, K. Watanabe, T. Taniguchi, M. Thiemens, F. Keilmann, G. C. Janssen, S. E. Zhu, P. Jarillo-Herrero, M. M. Fogler, and D. N. Basov, "Graphene on hexagonal boron nitride as a tunable hyperbolic metamaterial," *Nature Nanotechnology*, vol. 10, no. 8, pp. 682–686, 2015.

[4] F. Bonaccorso, Z. Sun, T. Hasan, and A. C. Ferrari, "Graphene photonics and optoelectronics," *Nature Photonics*, vol. 4, no. 9, pp. 611–622, 2010.

[5] B. Radisavljevic, A. Radenovic, J. Brivio, V. Giacometti, and A. Kis, "Single-layer MoS_2 transistors," *Nature Nanotechnology*, vol. 6, no. 3, pp. 147–150, 2011.

[6] L. Britnell, R. M. Ribeiro, A. Eckmann, R. Jalil, B. D. Belle, A. Mishchenko, Y. Kim, R. V. Gorbachev, T. Georgiou, S. V. Morozov, A. N. Grigorenko, A. K. Geim, C. Casiraghi, A. H. C. Neto, and K. S. Novoselov, "Strong Light-Matter Interactions Thin Films," *Science*, vol. 340, no. June, pp. 1311–1315, 2013.

[7] M. M. Furchi, D. K. Polyushkin, A. Pospischil, and T. Mueller, "Mechanisms of photoconductivity in atomically thin MoS_2," *Nano Letters*, vol. 14, no. 11, pp. 6165–6170, 2014.

[8] S. L. Howell, D. Jariwala, C. C. Wu, K. S. Chen, V. K. Sangwan, J. Kang, T. J. Marks, M. C. Hersam, and L. J. Lauhon, "Investigation of Band-Offsets at Monolayer-Multilayer MoS_2 Junctions by Scanning Photocurrent Microscopy," *Nano Letters*, vol. 15, no. 4, pp. 2278–2284, 2015.

[9] G. Aivazian, Z. Gong, a. M. Jones, R. L. Chu, J. Yan, D. G. Mandrus, C. Zhang, D. Cobden, W. Yao, and X. D. Xu, "Magnetic Control of Valley Pseudospin in Monolayer WSe_2," *Nature Physics*, vol. 1406, no. January, p. 2546, 2014.

[10] A. Srivastava, M. Sidler, A. V. Allain, D. S. Lembke, A. Kis, and A. Imamo, "Valley Zeeman effect in elementary optical excitations of monolayer WSe_2," *Nature Physics*, vol. 11, no. 2, pp. 141–147, 2015.

[11] Y. Ye, J. Xiao, H. Wang, Z. Ye, H. Zhu, M. Zhao, Y. Wang, J. Zhao, X. Yin, and X. Zhang, "Electrical generation and control of the valley carriers in a monolayer transition metal dichalcogenide," *Nature Nanotechnology*, vol. 11, no. 7, pp. 598–602, 2016.

[12] D. Xiao, M. C. Chang, and Q. Niu, "Berry phase effects on electronic properties," *Reviews of Modern Physics*, vol. 82, no. 3, pp. 1959–2007, 2010.

[13] Q. H. Wang, K. Kalantar-Zadeh, A. Kis, J. N. Coleman, and M. S. Strano, "Electronics and optoelectronics of two-dimensional transition metal dichalcogenides," *Nature Nanotechnology*, vol. 7, no. 11, pp. 699–712, 2012.

[14] F. Xia, H. Wang, D. Xiao, M. Dubey, and A. Ramasubramaniam, "Two-dimensional material nanophotonics," *Nature Photonics*, vol. 8, no. 12, pp. 899–907, 2014.

[15] F. H. L. Koppens, T. Mueller, P. Avouris, A. C. Ferrari, M. S. Vitiello, and M. Polini, "Photodetectors based on graphene, other two-dimensional materials and hybrid systems," *Nature Nanotechnology*, vol. 9, no. 10, pp. 780–793, 2014.

[16] W. Zhao, Z. Ghorannevis, K. K. Amara, J. R. Pang, M. Toh, X. Zhang, C. Kloc, P. H. Tan, and G. Eda, "Lattice dynamics in mono- and few-layer sheets of WS_2 and WSe_2," *Nanoscale*, vol. 5, no. 20, p. 9677, 2013.

[17] H. Zeng, G. B. Liu, J. Dai, Y. Yan, B. Zhu, R. He, L. Xie, S. Xu, X. Chen, W. Yao, and X. Cui, "Optical signature of symmetry variations and spin-valley coupling in atomically thin tungsten

dichalcogenides," *Scientific Reports*, vol. 3, no. 4, pp. 4908–4916, 2013.

[18] X. Zhang, X.-F. Qiao, W. Shi, J.-B. Wu, D.-S. Jiang, and P.-H. Tan, "Phonon and Raman scattering of two-dimensional transition metal dichalcogenides from monolayer, multilayer to bulk material," *Chemical Society Reviews*, vol. 44, pp. 2757–2785, 2015.

[19] M. S. El-Bana, D. Wolverson, S. Russo, G. Balakrishnan, D. M. K. Paul, and S. J. Bending, "Superconductivity in two-dimensional $NbSe_2$ field effect transistors," *Superconductor Science and Technology*, vol. 26, no. 12, 2013.

[20] K. F. Mak, C. Lee, J. Hone, J. Shan, and T. F. Heinz, "Atomically thin MoS_2: A new direct-gap semiconductor," *Physical Review Letters*, vol. 105, no. 13, pp. 2–5, 2010.

[21] E. Courtade, M. Semina, M. Manca, M. M. Glazov, C. Robert, F. Cadiz, G. Wang, T. Taniguchi, K. Watanabe, M. Pierre, W. Escoffier, E. L. Ivchenko, P. Renucci, X. Marie, T. Amand, and B. Urbaszek, "Charged excitons in monolayer WSe_2: Experiment and theory," *Physical Review B*, vol. 96, no. 8, pp. 1–12, 2017.

[22] A. Splendiani, L. Sun, Y. Zhang, T. Li, J. Kim, C. Y. Chim, G. Galli, and F. Wang, "Emerging photoluminescence in monolayer MoS_2," *Nano Letters*, vol. 10, no. 4, pp. 1271–1275, 2010.

[23] J. Pei, J. Yang, R. Xu, Y. H. Zeng, Y. W. Myint, S. Zhang, J. C. Zheng, Q. Qin, X. Wang, W. Jiang, and Y. Lu, "Exciton and Trion Dynamics in Bilayer MoS_2," *Small*, vol. 11, no. 48, pp. 6384–6390, 2015.

[24] P. Kusch, S. Mastel, N. S. Mueller, N. Morquillas Azpiazu, S. Heeg, R. Gorbachev, F. Schedin, U. Hübner, J. I. Pascual, S. Reich, and R. Hillenbrand, "Dual-Scattering Near-Field Microscope for Correlative Nanoimaging of SERS and Electromagnetic Hotspots," *Nano Letters*, vol. 17, no. 4, pp. 2667–2673, 2017.

[25] D. A. Neamen, *Semiconductor physics and devices*.

[26] C. C. J.-P. Colinge, *Physics of Semiconductor Devices*.

[27] A. Di Bartolomeo, "Graphene Schottky diodes: An experimental review of the rectifying graphene/semiconductor heterojunction," *Physics Reports*, vol. 606, no. January, pp. 1–58, 2016.

[28] S. M. Sze and K. Kwok, *Physics of Semiconductor Devices*. No. 1, 2007.

[29] S. M. Sze, "Physics of Semiconductor Devices," 1969.

[30] C. C. Wu, D. Jariwala, V. K. Sangwan, T. J. Marks, M. C. Hersam, and L. J. Lauhon, "Elucidating the photoresponse of ultrathin MoS_2 field-effect transistors by scanning photocurrent microscopy," *Journal of Physical Chemistry Letters*, vol. 4, no. 15, pp. 2508–2513, 2013.

[31] M. McColl, M. F. Millea, and A. H. Silver, "The superconductor-semiconductor Schottky barrier diode detector," *Applied Physics Letters*, vol. 23, no. 5, pp. 263–264, 1973.

[32] L. Vernon, "The Super-Schottky Diode," vol. M, no. 4, pp. 286–294, 1977.

[33] A. Savin, M. Prunnila, J. Ahopelto, P. Kivinen, P. Törmä, and J. Pekola, "Application of superconductor-semiconductor Schottky barrier for electron cooling," *Physica B: Condensed Matter*, vol. 329-333, no. II, pp. 1481–1484, 2003.

[34] Y.-J. Doh, "Tunable Supercurrent Through Semiconductor Nanowires," *Science*, vol. 309, no. 5732, pp. 272–275, 2005.

[35] V. Rodov and A. Ankoudinov, "Super Barrier Rectifier - A New Generation of Power Diode," *Industry Applications, IEEE*, vol. 44, no. 1, pp. 234–237, 2008.

[36] Y. P. Shim and C. Tahan, "Bottom-up superconducting and Josephson junction devices inside a group-IV semiconductor," *Nature Communications*, vol. 5, no. May, pp. 1–8, 2014.

[37] D. Montemurro, D. Massarotti, P. Lucignano, S. Roddaro, D. Stornaiuolo, D. Ercolani, L. Sorba, A. Tagliacozzo, F. Beltram, and F. Tafuri, "Towards a Hybrid High Critical Temperature Superconductor Junction With a Semiconducting InAs Nanowire Barrier," *Journal of Superconductivity and Novel Magnetism*, vol. 28, no. 12, pp. 3429–3437, 2015.

[38] K. F. Mak, K. He, J. Shan, and T. F. Heinz, "Control of valley polarization in monolayer MoS_2 by optical helicity," *Nature Nanotechnology*, vol. 7, no. 8, pp. 494–498, 2012.

[39] T. Low and F. Guinea, "Strain-induced pseudomagnetic field for novel graphene electronics," *Nano Letters*, vol. 10, no. 9, pp. 3551–3554, 2010.

[40] N. Levy, S. A. Burke, K. L. Meaker, M. Panlasigui, A. Zettl, F. Guinea, A. H. Castro Neto, M. F. Crommie, "Strain-Induced Pseudo - Magnetic Fields Greater Than 300 Tesla in Graphene Nanobubbles," *Science*, no. July, pp. 544–547, 2010.

[41] H. T. Yang, "Strain induced shift of Dirac points and the pseudo-magnetic field in graphene," *Journal of Physics Condensed Matter*, vol. 23, no. 50, 2011.

[42] T. M. L. Yeh, N. C., S. Yeom, B. L. Standley, R. T. P. Wu, D. A. Boyd, and M. W. Bockrath, "Strain-induced pseudo-magnetic fields and charging effects on CVD-grown graphene," *Surface Science*, vol. 605, no. 17-18, pp. 1649–1656, 2011.

[43] D. B. Zhang, G. Seifert, and K. Chang, "Strain-induced pseudomagnetic fields in twisted graphene nanoribbons," *Physical Review Letters*, vol. 112, no. 9, pp. 1–5, 2014.

[44] Y. Jiang, J. Mao, J. Duan, X. Lai, K. Watanabe, T. Taniguchi, and E. Y. Andrei, "Visualizing Strain-Induced Pseudomagnetic Fields in Graphene through an hBN Magnifying Glass," *Nano Letters*, vol. 17, no. 5, pp. 2839–2843, 2017.

[45] J. Kang, W. Cao, X. Xie, D. Sarkar, W. Liu, and K. Banerjee, "Graphene and beyond-graphene 2D crystals for next-generation green electronics," vol. 9083, p. 908305, 2014.

[46] T. Shapoval, H. Stopfel, S. Haindl, J. Engelmann, D. S. Inosov, B. Holzapfel, V. Neu, and L. Schultz, "Quantitative assessment of pinning forces and magnetic penetration depth in NbN thin films from complementary magnetic force microscopy and transport measurements," *Physical Review B - Condensed Matter and Materials Physics*, vol. 83, no. 21, pp. 1–7, 2011.

[47] M. Timmermans, T. Samuely, B. Raes, J. Van De Vondel, and V. V. Moshchalkov, "Observing vortex motion on $NbSe_2$ with STM," *Physica C: Superconductivity and its Applications*, vol. 503, pp. 154–157, 2014.

[48] M. M. Ugeda, A. J. Bradley, Y. Zhang, S. Onishi, Y. Chen, W. Ruan, C. Ojeda-Aristizabal, H. Ryu, M. T. Edmonds, H. Z. Tsai, A. Riss, S. K. Mo, D. Lee, A. Zettl, Z. Hussain, Z. X. Shen, and M. F. Crommie, "Characterization of collective ground states in single-layer $NbSe_2$," *Nature Physics*, vol. 12, no. 1, pp. 92–97, 2016.

[49] F. S. O. Toshihiro Shimada and B. A. Parkinsion *Jpn. J. Appl. Phys.*, vol. 33, no. 5A, pp. 2696–2698, 1994.

[50] F. K. Hölzl, J.; Schulte, *Work function of metals.* 1979.

[51] A. Potts, P. Brigden, D. Law, and E. Lee, "Photoelectron spectroscopy of solids using gas-phase spectrometers," *Journal of Electron Spectroscopy and Related Phenomena*, vol. 24, no. 2, pp. 267–281, 1981.

[52] A. Volodin, K. Temst, C. Van Haesendonck, and Y. Bruynseraede, "Imaging of vortices in conventional superconductors by magnetic force microscopy," *Physica C: Superconductivity and its Applications*, vol. 332, no. 1, pp. 156–159, 2000.

[53] A. Volodin, K. Temst, C. Van Haesendonck, and Y. Bruynseraede, "Low temperature magnetic force microscopy with enhanced sensitivity based on piezoresistive detection," *Review of Scientific Instruments*, vol. 71, no. 2000, p. 4468, 2000.

[54] Y. B. Alexander Volodin, Kristiaan Temst, Chris Van Haesendonck, "Magnetic force microscopy on superconducting $NbSe_2$ and Nb surfaces," *Physica B: Condensed Matter*, vol. 284-288, pp. 815–816, 2000.

[55] J. R. Kirtley, "Fundamental studies of superconductors using scanning magnetic imaging," *Reports on Progress in Physics*, vol. 73, no. 12, 2010.

[56] R. L.Price and W. G. J. Jerome, *Basic Confocal microscopy*. 2011.

[57] S. W. Paddock, *Confocal microscopy*, vol. 122. 1999.

[58] J. B. Pawley, *Handbook of biological confocal microscopy*. 1990.

[59] K. Komider, J. W. González, and J. Fernández-Rossier, "Large spin splitting in the conduction band of transition metal dichalcogenide monolayers," *Physical Review B - Condensed Matter and Materials Physics*, vol. 88, no. 24, pp. 1–7, 2013.

[60] J. P. Echeverry, B. Urbaszek, T. Amand, X. Marie, and I. C. Gerber, "Splitting between bright and dark excitons in transition metal dichalcogenide monolayers," *Physical Review B*, vol. 93, no. 12, pp. 1–5, 2016.

[61] M. R. Molas, C. Faugeras, A. O. Slobodeniuk, K. Nogajewski, M. Bartos, D. M. Basko, and M. Potemski, "Brightening of dark excitons in monolayers of semiconducting transition metal dichalcogenides," *2D Materials*, vol. 4, no. 2, 2017.

[62] G. Wang, C. Robert, A. Suslu, B. Chen, S. Yang, S. Alamdari, C. Gerber, T. Amand, X. Marie, S. Tongay, and B. Urbaszek, "Spin-orbit engineering in transition metal dichalcogenide alloy monolayers," *Nature Communications*, vol. 6, pp. 1–9, 2015.

[63] T. Yan, X. Qiao, X. Liu, P. Tan, and X. Zhang, "Photoluminescence properties and exciton dynamics in monolayer WSe2," *Applied Physics Letters*, vol. 105, no. 10, p. 101901, 2014.

[64] G. Plechinger, P. Nagler, A. Arora, R. Schmidt, A. Chernikov, A. G. del Águila, P. C. Christianen, R. Bratschitsch, C. Schüller, and T. Korn, "Trion fine structure and coupled spin-valley dynamics in monolayer tungsten disulfide," *Nature Communications*, vol. 7, no. May, p. 12715, 2016.

[65] A. Arora, M. Koperski, K. Nogajewski, J. Marcus, C. Faugeras, and M. Potemski, "Excitonic resonances in thin films of WSe2: From monolayer to bulk material," pp. 10421–10429, 2015.

[66] Y. Chen, W. Wen, Y. Zhu, N. Mao, Q. Feng, M. Zhang, H.-P. Hsu, J. Zhang, Y.-S. Huang, and L. Xie, "Temperature-dependent photoluminescence emission and Raman scattering from $Mo_{1-x}W_xS_2$ monolayers," *Nanotechnology*, vol. 27, no. 44, p. 445705, 2016.

[67] J. Huang, T. B. Hoang, and M. H. Mikkelsen, "Probing the origin of excitonic states in monolayer WSe_2," *Scientific Reports*, vol. 6, no. August 2015, pp. 1–7, 2016.

[68] M. D. Tran, J. H. Kim, and Y. H. Lee, "Tailoring photoluminescence of monolayer transition metal dichalcogenides," *Current Applied Physics*, vol. 16, no. 9, pp. 1159–1174, 2016.

[69] J. Quereda, A. Castellanos-Gómez, N. Agraït, and G. Rubio-Bollinger, "Single-layer MoS_2 roughness and sliding friction quenching by interaction with atomically flat substrates," *Applied Physics Letters*, vol. 105, no. 5, pp. 1–10, 2014.

[70] Q. Wang, Y. Li, B. Bai, W. Mao, Z. Wang, and N. Ren, "Effects of silicon dioxide surface roughness on Raman characteristics and mechanical properties of graphene," *RSC Adv.*, vol. 4, no. 98, pp. 55087–55093, 2014.

[71] C. H. Lui, L. Liu, K. F. Mak, G. W. Flynn, and T. F. Heinz, "Ultraflat graphene," *Nature*, vol. 462, no. 7271, pp. 339–341, 2009.

[72] D. Hill, X. Blasco, M. Porti, M. Nafría, and X. Aymerich, "Characterising the surface roughness of AFM grown SiO_2 on Si," *Microelectronics Reliability*, vol. 41, no. 7, pp. 1077–1079, 2001.

[73] E. A. Irene, "Ultra-thin SiO2film studies: Index, thickness, roughness and the initial oxidation regime," *Solid-State Electronics*, vol. 45, no. 8, pp. 1207–1217, 2001.

[74] C. R. Ronda, *Luminescence: From Theory to Applications*. 2007.

[75] P. Viste, J. Plain, R. Jaffiol, A. Vial, P. M. Adam, and P. Royer, "Enhancement and quenching regimes in metal-semiconductor hybrid optical nanosources," *ACS Nano*, vol. 4, no. 2, pp. 759–764, 2010.

[76] V. N. Pustovit and T. V. Shahbazyan, "Fluorescence quenching near small metal nanoparticles," pp. 1–7.

[77] M. Haridas, L. N. Tripathi, and J. K. Basu, "Photoluminescence enhancement and quenching in metal-semiconductor quantum dot hybrid arrays," *Applied Physics Letters*, vol. 98, no. 6, pp. 2009–2012, 2011.

[78] M. S. Mehata, "Enhancement of Charge Transfer and Quenching of Photoluminescence of Capped CdS Quantum Dots," *Scientific Reports*, vol. 5, no. May, pp. 1–11, 2015.

[79] X. Yin, Y. Li, F. Ke, C. Lin, H. Zhao, L. Gan, Z. Luo, R. Zhao, T. F. Heinz, and Z. Hu, "Evolution of the Raman spectrum of graphene grown on copper upon oxidation of the substrate," *Nano Research*, vol. 7, no. 11, pp. 1613–1622, 2014.

[80] N. E. Staley, J. Wu, P. Eklund, Y. Liu, L. Li, and Z. Xu, "Electric field effect on superconductivity in atomically thin flakes of $NbSe_2$," *Physical Review B - Condensed Matter and Materials Physics*, vol. 80, no. 18, pp. 1–6, 2009.

[81] B. X. Huang, K. Wang, J. S. Church, and Y. S. Li, "Characterization of oxides on niobium by raman and infrared spectroscopy," *Electrochimica Acta*, vol. 44, no. 15, pp. 2571–2577, 1999.

[82] S. Choi, Z. Shaolin, and W. Yang, "Layer-number-dependent work function of MoS_2 nanoflakes," *Journal of the Korean Physical Society*, vol. 64, no. 10, pp. 1550–1555, 2014.

[83] S. S. Baik, S. Im, and H. J. Choi, "Work Function Tuning in Two-Dimensional MoS_2 Field-Effect-Transistors with Graphene and Titanium Source-Drain Contacts," *Scientific Reports*, vol. 7, no. March, pp. 1–8, 2017.

[84] P. Zhou, X. Song, X. Yan, C. Liu, and L. Chen, "Controlling the work function of molybdenum disul fi de by in situ metal deposition," *Nanotechnology*, vol. 27, no. 34, pp. 1–7.

[85] I. Goykhman, U. Sassi, B. Desiatov, N. Mazurski, S. Milana, D. De Fazio, A. Eiden, J. Khurgin, J. Shappir, U. Levy, and A. C. Ferrari, "On-Chip Integrated, Silicon-Graphene Plasmonic Schottky Photodetector with High Responsivity and Avalanche Photogain," *Nano Letters*, vol. 16, no. 5, pp. 3005–3013, 2016.

[86] A. Di Bartolomeo, G. Luongo, L. Iemmo, and F. Giubileo, "Graphene-Silicon Schottky diodes for photodetection," *arXiv*, no. 1710.10142, 2017.

[87] Z. Yin, H. Li, H. Li, L. Jiang, Y. Shi, Y. Sun, G. Lu, Q. Zhang, X. Chen, and H. Zhang, "Single-layer MoS_2 phototransistors," *ACS Nano*, vol. 6, no. 1, pp. 74–80, 2012.

[88] A. K. Newaz, D. Prasai, J. I. Ziegler, D. Caudel, S. Robinson, R. F. Haglund, and K. I. Bolotin, "Electrical control of optical properties of monolayer MoS_2," *Solid State Communications*, vol. 155, pp. 49–52, 2013.

[89] K. Cho, T. Y. Kim, W. Park, J. Park, D. Kim, J. Jang, H. Jeong, S. Hong, and T. Lee, "Gate-bias stress-dependent photoconductive characteristics of multi-layer MoS_2 field-effect transistors," *Nanotechnology*, vol. 25, no. 15, 2014.

[90] A. Castellanos-Gomez, R. Roldán, E. Cappelluti, M. Buscema, F. Guinea, H. S. J. Van Der Zant, and G. A. Steele, "Local strain engineering in atomically thin MoS_2," *Nano Letters*, vol. 13, no. 11, pp. 5361–5366, 2013.

[91] J. Quereda, J. J. Palacios, N. Agräit, A. Castellanos-Gomez, and G. Rubio-Bollinger, "Strain engineering of Schottky barriers in single- and few-layer MoS_2 vertical devices," *2D Materials*, vol. 4, no. 2, 2017.

[92] H. Kroemer, "Heterostructure devices: A device physicist looks at interfaces," *Surface Science*, vol. 132, no. 1-3, pp. 543–576, 1983.

[93] W. S. Yun, S. W. Han, S. C. Hong, I. G. Kim, and J. D. Lee, "Thickness and strain effects on electronic structures of transition metal dichalcogenides: 2H-MX_2 semiconductors (M = Mo, W; X = S, Se, Te)," *Physical Review B*, vol. 85, no. 3, p. 033305, 2012.

[94] Z. Ahmad and M. H. Sayyad, "Electrical characteristics of a high rectification ratio organic Schottky diode based on methyl red," *Optoelectronics and Advanced Materials, Rapid Communications*, vol. 3, no. 5, pp. 509–512, 2009.

[95] S. Das and J. Appenzeller, "Screening and interlayer coupling in multilayer MoS_2," *Physica Status Solidi - Rapid Research Letters*, vol. 7, no. 4, pp. 268–273, 2013.

[96] A. K. M. Newaz, D. Prasai, J. I. Ziegler, D. Caudel, S. Robinson, R. F. Haglund, and K. I. Bolotin, "Electrical Control of Optical Properties of Monolayer MoS_2," vol. 2, pp. 1–5, 2012.

[97] S. Schmitt-Rink, D. S. Chemla, and D. A. Miller, "Theory of transient excitonic optical nonlinearities in semiconductor quantum-well structures," *Physical Review B*, vol. 32, no. 10, pp. 6601–6609, 1985.

[98] M. Y. Li, C. H. Chen, Y. Shi, and L. J. Li, "Heterostructures based on two-dimensional layered materials and their potential applications," *Materials Today*, vol. 19, no. 6, pp. 322–335, 2016.

[99] M. M. Furchi, A. A. Zechmeister, F. Hoeller, S. Wachter, A. Pospischil, and T. Mueller, "Photovoltaics in Van der Waals Heterostructures," *IEEE Journal of Selected Topics in Quantum Electronics*, vol. 23, no. 1, 2017.

[100] J. Wang, F. Ma, and M. Sun, "Graphene, hexagonal boron nitride, and their heterostructures: properties and applications," *RSC Adv.*, vol. 7, no. 27, pp. 16801–16822, 2017.

[101] N. Huo, Y. Yang, and J. Li, "Optoelectronics based on 2D TMDs and heterostructures," *Journal of Semiconductors*, vol. 38, no. 3, 2017.

[102] C. Chen, C. Maria, C. Zhang, J. Song, and C. Chen, "Electronic structure of graphene / hexagonal boron nitride heterostructure revealed by Nano-ARPES Electronic structure of graphene / hexagonal boron nitride heterostructure revealed by NanoARPES," *Journal of Physics*, no. 864, p. 012005, 2017.

[103] E. V. Calman, M. M. Fogler, L. V. Butov, S. Hu, A. Mishchenko, and A. K. Geim, "Indirect excitons in van der Waals heterostructures at room temperature," *Nature Communications*, vol. 9, pp. 1–5, 2018.

[104] Q. Zeng and Z. Liu, "Novel Optoelectronic Devices: Transition-Metal-Dichalcogenide-Based 2D Heterostructures," *Advanced Electronic Materials*, vol. 4, no. 2, pp. 1–20, 2018.

[105] Rui Cheng, Shan Jiang, Yu Chen, Yuan Liu, Nathan Weiss, Hung-Chieh Cheng, Hao Wu, Yu Huang, and Xiangfeng Duan, "Few-layer molybdenum disulfide transistors and circuits for high-speed flexible electronics," *Nat Commun*, vol. 14, no. 5, p. 51143, 2014.

[106] B. W. Baugher, H. O. Churchill, Y. Yang, and P. Jarillo-Herrero, "Optoelectronic devices based on electrically tunable p-n diodes in a monolayer dichalcogenide," *Nature Nanotechnology*, vol. 9, no. 4, pp. 262–267, 2014.

[107] C. M. Torres, Y. W. Lan, C. Zeng, J. H. Chen, X. Kou, A. Navabi, J. Tang, M. Montazeri, J. R. Adleman, M. B. Lerner, Y. L. Zhong,

L. J. Li, C. D. Chen, and K. L. Wang, "High-Current Gain Two-Dimensional MoS2-Base Hot-Electron Transistors," *Nano Letters*, vol. 15, no. 12, pp. 7905–7912, 2015.

[108] P. Agnihotri, P. Dhakras, and J. U. Lee, "Bipolar Junction Transistors in Two-Dimensional WSe_2 with Large Current and Photocurrent Gains," *Nano Letters*, vol. 16, no. 7, pp. 4355–4360, 2016.

[109] C. Y. Lin, X. Zhu, S. H. Tsai, S. P. Tsai, S. Lei, Y. Shi, L. J. Li, S. J. Huang, W. F. Wu, W. K. Yeh, Y. K. Su, K. L. Wang, and Y. W. Lan, "Atomic-Monolayer Two-Dimensional Lateral Quasi-Heterojunction Bipolar Transistors with Resonant Tunneling Phenomenon," *ACS Nano*, vol. 11, no. 11, pp. 11015–11023, 2017.

[110] C. Kim, I. Moon, D. Lee, M. S. Choi, F. Ahmed, S. Nam, Y. Cho, H. J. Shin, S. Park, and W. J. Yoo, "Fermi Level Pinning at Electrical Metal Contacts of Monolayer Molybdenum Dichalcogenides," *ACS Nano*, vol. 11, no. 2, pp. 1588–1596, 2017.

[111] Y. Liu, P. Stradins, and S.-h. Wei, "Van der Waals metal â^' semiconductor junction : Weak Fermi level pinning enables effective tuning of Schottky barrier," *Science Advances*, vol. 2, no. 1, p. e1600069, 2016.

[112] C. Gong, L. Colombo, R. M. Wallace, and K. Cho, "The unusual mechanism of partial fermi level pinning at metal-MoS_2 interfaces," *Nano Letters*, vol. 14, no. 4, pp. 1714–1720, 2014.

[113] H. Zhong, R. Quhe, Y. Wang, Z. Ni, M. Ye, Z. Song, Y. Pan, J. Yang, L. Yang, M. Lei, J. Shi, and J. Lu, "Interfacial Properties of Monolayer and Bilayer MoS_2 Contacts with Metals: Beyond the Energy Band Calculations," *Scientific Reports*, vol. 6, no. March, pp. 1–16, 2016.

[114] Y. Zhao, X. Xiao, Y. Huo, Y. Wang, T. Zhang, K. Jiang, J. Wang, S. Fan, and Q. Li, "Influence of Asymmetric Contact Form on Contact Resistance and Schottky Barrier, and Corresponding Applications of Diode," *ACS Applied Materials and Interfaces*, vol. 9, no. 22, pp. 18945–18955, 2017.

[115] W. Wang, Y. Liu, L. Tang, Y. Jin, T. Zhao, and F. Xiu, "Controllable Schottky barriers between MoS_2 and permalloy," *Scientific Reports*, vol. 4, pp. 1–6, 2014.

[116] R. Schmidt, A. Arora, G. Plechinger, P. Nagler, A. Granados Del Águila, M. V. Ballottin, P. C. M. Christianen, S. Michaelis De Vasconcellos, C. Schüller, T. Korn, and R. Bratschitsch, "Magnetic-

Field-Induced Rotation of Polarized Light Emission from Monolayer WS_2," *Physical Review Letters*, vol. 117, no. 7, pp. 1–6, 2016.

[117] L. Pietrobon, L. Fallarino, A. Berger, A. Chuvilin, F. Casanova, and L. E. Hueso, "Weak Delocalization in Graphene on a Ferromagnetic Insulating Film," *Small*, vol. 11, no. 47, pp. 6295–6301, 2015.

[118] Y. Li, J. Ludwig, T. Low, A. Chernikov, X. Cui, G. Arefe, Y. D. Kim, A. M. Van Der Zande, A. Rigosi, H. M. Hill, S. H. Kim, J. Hone, Z. Li, D. Smirnov, and T. F. Heinz, "Valley splitting and polarization by the zeeman effect in monolayer $MoSe_2$," *Physical Review Letters*, vol. 113, no. 26, pp. 1–5, 2014.

[119] M. Koperski, K. Nogajewski, A. Arora, V. Cherkez, P. Mallet, J. Y. Veuillen, J. Marcus, P. Kossacki, and M. Potemski, "Single photon emitters in exfoliated WSe_2 structures," *Nature Nanotechnology*, vol. 10, no. 6, pp. 503–506, 2015.

[120] D. Macneill, C. Heikes, K. F. Mak, Z. Anderson, A. Kormányos, V. Zólyomi, J. Park, and D. C. Ralph, "Breaking of valley degeneracy by magnetic field in monolayer $MoSe_2$," *Physical Review Letters*, vol. 114, no. 3, pp. 1–5, 2015.

[121] T. Smolenski, M. Goryca, M. Koperski, C. Faugeras, T. Kazimierczuk, A. Bogucki, K. Nogajewski, P. Kossacki, and M. Potemski, "Tuning valley polarization in a WSe_2 monolayer with a tiny magnetic field," *Physical Review X*, vol. 6, no. 2, pp. 1–7, 2016.

[122] C. Hauser, T. Richter, N. Homonnay, C. Eisenschmidt, M. Qaid, H. Deniz, D. Hesse, M. Sawicki, S. G. Ebbinghaus, and G. Schmidt, "Yttrium Iron Garnet Thin Films with Very Low Damping Obtained by Recrystallization of Amorphous Material," *Scientific Reports*, vol. 6, no. June 2015, pp. 1–8, 2016.

[123] H. Orucu, G. Ozen, J. Collins, and B. Di Bartolo, "Temperature dependence of the luminescence spectra of garnet crystals doped with chromium ions," *Optical Materials*, vol. 31, no. 7, pp. 1065–1070, 2009.

[124] B. Struve and G. Huber, "The Effect of the Crystal Field Strength on the Optical Spectra of Cr^{3+} in Gallium Garnet Laser Crystals," *Applied Physics B*, vol. 36, no. 1985, pp. 195–201, 2000.

Nieves Morquillas Azpiazu

Bilbao (SPAIN), 07 February 1990

Email yasazni@gmail.com Phone (M) +34 60 834 073

Academic and professional background

2014-Current

PhD in Physics, CIC nanoGUNE, San Sebastian
Optoelectronics, Valleytronics, 2D materials

2017

Supervision of Bachelor student. "Accessing the valley degree of freedom in WS_2".

2015

Research Stay, Freie Universität Berlin (FUB), Germany

Supervision of Bachelor student: "Optoelectronics in two-dimensional materials".

2013-2014

MSc in Nanoscience and Nanotechnology. Universidad del País Vasco (UPV/EHU). Grade: 8.22

"Confocal Raman spectro-microscopy of layered materials".
Supervisor: J.I. Pascual. Grade: 9

2013

Internship in Tecnalia Research and Inovation, INASMET Energy and Environment Division.

2008-2013

Licenciatura en Química, Universidad del País Vasco (UPV/EHU). Grade: 6.98

2012-2013

Research project, Condensed Matter and Interface group (CMI), Debye Institute, Utrecht University (UU), The Netherlands. Erasmus grant

"Upconversion Luminescence in Gd_2O_2S and $LiYF_4$ microcrystals doped with lanthanides".
Supervisor: Prof. Dr. Andries Meijerink, Dr. Rosa Martín Rodríguez. Grade: 8

2011-2012

SENECA grant, Universidad Santiago de Compostela (USC).
CUM LAUDE: Garantía de calidad y gestión de laboratorios.

Publications

"Dual-scattering near-field microscope for correlative nanoimaging of SERS and electromagnetic hotspots". **NanoLetters**, 17 (4), pp 2667-2673

"Combined Tip-Enhanced Raman Spectroscopy and Scattering- type scanning near-field optical microscopy". *(Submitted to Journal of Physical Chemistry)*

Languages

Spanish - **Native** English - **Advanced (CAE, C1)** French/Basque - **Basic**

Seminars/Conferences

2018 May	MATLAB for Research. **Attendance**
2018 Mar	DPG 2018 (Meeting of the German Physics Society): "Tuning optoelectronic properties in transition metal dichalcogenides". **Poster** presentation
2018 Jan	GEFES 2018 (Meeting of the Division de Física de la Materia Condensada Española): "Tuning optoelectronic properties in transition metal dichalcogenides". **Poster** presentation
2017 Nov	nanoGUNE seminar: "Optoelectronic properties in 2D junctions". **Oral** presentation
2017 Jan	2nd nanoGUNE PhD workshop. **Organization** and attendance
2016 May	European Conference in NanoFilms (ECNF 2016): "Potential Barriers on 2D materials devices". **Oral** presentation
2016 May	nanoGUNE seminar: "Optoelectronics in a semiconductor-superconductor transition metal dichalcogenide hybrid". **Oral** presentation.
2016 Jan	GEFES 2016 (Meeting of the Division de Física de la Materia Condensada Española): "Tuning optoelectronic properties in transition metal dichalcogenides". **Poster** presentation.
2016 Jan	1st nanoGUNE PhD workshop. **Organization** and attendance.
2015 Jul-Aug	"Optoelectronics in two-dimensional materials". **Supervision** of Bachelor student:
2015 Jul	New Trend in Topological Insulators (NTTI 2016): "Search for Majorana Modes in superconductor heterostructures". (2nd author) **Poster** presentation.
2015 Jan	nanoGUNE open day: "Studying the local properties of novel materials at low temperatures". **Poster** presentation.

Working Skills

Computer	LabVIEW - Igor - LATEX – Matlab - SPSS - Gaussian01 - Spartan - Statgraphics - OSX - MS Office
Techniques	Spectroscopic techniques - Electric transport - Atomic and Magnetic Force microscopy - Near Field Optics – Cryogenics
Other	Music studies (Clarinet) – Sailing (Instructor, Race Committee)

Publications

Dual-Scattering Near-Field Microscope for Correlative Nanoimaging of SERS and Electromagnetic Hotspots
Patryk kusch, Stefan Mastel, Niclas S. Mueller, Nieves Morquillas Azpiazu, Sebastian Heeg, Roman Gorbachev, Fredrik Schedin, Uwe Hubner, J.I. Pascual, Stephanie Reich, Rainer Hillenbrand.
Nanoletters, **17**, 2667-2673 (2017)

Combined Tip-Enhanced Raman Spectroscopy and Scattering-type scanning near field optical microscopy
Patryk kusch, Nieves Morquillas Azpiazu, Niclas S. Mueller, Stefan Mastel, J.I. Pascual and Rainer Hillenbrand.
Submitted to Journal of Physical Chemistry (2018)